Summer 8-2012

Analysis of Fiber Bragg Gratings For Ultrasonic Detection

Tongqing Liu
University of Nebraska-Lincoln, tongqing@huskers.unl.edu

ANALYSIS OF FIBER BRAGG GRATINGS FOR ULTRASONIC DETECTION

by

Tongqing Liu

A THESIS

Presented to the Faculty of

The Graduate College at the University of Nebraska

In Partial Fulfilment of Requirements

For the Degree of Master of Science

Major: Electrical Engineering

Under the Supervision of Professor Ming Han

Lincoln, Nebraska

August, 2012

ANALYSIS OF FIBER BRAGG GRATINGS FOR ULTRASONIC DETECTION

Tongqing Liu, M.S.

University of Nebraska, 2012

Adviser: Ming Han

Fiber optic sensors became an emerging technique to detect ultrasonic emissions in the last decade. Their light weight, immunity to electromagnetic interference and capacity of being multiplexed make them defeat their electronic counterparts in various applications. In this thesis we presented a novel fiber optic ultrasonic sensor based on π-phase shift fiber Bragg gratings. Numerical simulations were performed to study the characteristics of π-phase shift fiber Bragg gratings impinged by ultrasonic waves. The coupling theory was introduced to analyze the change of fiber Bragg gratings when impinged by ultrasonic waves, and the transfer matrix method was utilized to implement the simulation. In addition, the effect of the grating length and grating refractive index modification depth on the wavelength sensitivity and intensity sensitivity of the π-phase shift fiber Bragg grating sensors were investigated. The responses of π-phase shift fiber Bragg gratings under ultrasonic pressure waves were also compared with that of uniform fiber gratings. Finally, the responses of πFBGs when impinged by ultrasonic longitudinal waves and shear waves were provided. Our analysis revealed several unique characteristics of π-phase shift fiber Bragg gratings used for ultrasonic detection and will be useful for design and optimization of fiber optic ultrasonic sensors with π-phase shift fiber Bragg grating as the sensing element.

ACKNOWLEDGMENTS

Foremost, I would like to express my sincere gratitude to my thesis advisor, Professor Ming Han, who provides me this great opportunity to study and work in this dynamic group and cutting-edge research area. His profound knowledge, broad vision, and hardworking attitude have a significant impact on my career path. I have not only learnt how to deal with problems in experiments, analyze numerically, and write technical papers, but also how to think creatively and be an efficient researcher.

I am grateful to my committee members, Professor Dennis R. Alexander and Professor Natale J. Ianno, for serving on my committee and reviewing my thesis.

I would also like to thank the colleagues in our group, Fawen Guo, Thomas Fink, and Qi Zhang. Thank you for helping me improve experiments, as well as giving me valuable advices which inspire me a lot. In addition, I would like to acknowledge the contribution of my collaborator Craig Zuhlke for his assistance in femtosecond laser experiment. Working on that project deepens my understanding of various kinds of laser systems. My gratitude also goes to Nicholas Rowse, John Bruce III, and Troy Anderson for your help when I was working in their lab. I would like to thank my friends here in Lincoln, including Li He, Zhe Zhang, Jinya Pu, Yang Gao, and Qing Chen, for offering your hands when I need you most. It is a great honor to have been with them during the past three years.

Finally, I would like to convey my great appreciation to my families for their love, understanding, and encouragement during my study at University of Nebraska-Lincoln. Without their support, I would not be where I am now.

The work is supported by Office of Naval Research under grant number N00014111026 and China Scholarship Council.

Contents

List of Figures

List of Tables

Nomenclature

β	The propagation constant of light
ϵ	The strain vector
$\frac{1}{n^2}$	The optical indicatrix of the fiber
$\hat{\sigma}$	The general dc coupling coefficient
κ	The ac coupling
Λ	The period of the FBG structure
λ_B	Bragg wavelength
λ_s	The wavelength of ultrasonic wave
ν	Poisson's ratio
ω	The angular frequency of ultrasonic wave
σ	The stress vector
D	The diameter of the fiber
E	Young's modulus of the fiber
n	Effective refractive index of optical mode

P_0	The peak pressure of ultrasonic wave
p_{11}	1,1 element of strain-optic tensor
p_{12}	1,2 element of strain-optic tensor
$R(z)$	The amplitude of forward-propagating mode
$S(z)$	The amplitude of backward-propagating mode

Chapter 1

Introduction

1.1 Motivation of the Work

Ultrasonic emission is an important indicator of material degradation in structural health monitoring (SHM), as acoustic signals in the form of ultrasonic waves are generated and propagate in a structure when cracks occur, defects grow, or surface degrades [1][2][3][4]. Also, ultrasonic waves can be generated actively in order to detect and evaluate the flaws occurring in a structure in the case of ultrasound-based nondestructive testing (NDT) [5][6][7]. Thus, ultrasonic detection has been of a great interest in the applications like SHM and NDT. Traditionally, ultrasonic testing uses the piezoelectric ceramics for ultrasonic detectors [3]. In the last two decades, fiber optic sensors are widely investigated in the applications of sensing temperature [8] [9], strain [10] [11], pressure [12] [13], electric field [14] [15], magnetic field [16] and ultrasonic waves [17][18]. Fiber optic ultrasonic sensors offer numerous advantages over their electronic counterparts when they are applied to SHM [19][20][21][22]. First, they are immune to electromagnetic interference (EMI), since the fiber is not electrically conductive. Second, fiber-optic sensors feature small size and light weight, and

can be easily embedded into the structure without affecting the mechanical properties of the structure. Third, fiber-optic sensors, particularly those based on fiber Bragg grating (FBG)[23][1][2], offer excellent multiplexing capabilities, making them ideal for application involving sensing at multiple locations. Both wavelength-domain multiplexing and time-domain multiplexing can be used to achieve multiplexed fiber-optic sensing [24] [25] [26].

Due to these remarkable advantages, FBG-based ultrasonic sensing has become an active research area in the past decade for structural health monitoring. Two different schemes have been proposed to detect ultrasonic waves using FBG sensors [27]. The first one relies on detecting the spectral shift of the Bragg wavelength caused by the strains of the ultrasonic waves, in which case the broadband laser is used [28] [29]. The second one is to monitor the ultrasonic-induced reflectivity variation of FBG using a narrowband tunable laser source. In this case the laser is tuned to the wavelength for which the reflectivity from the Bragg grating is roughly half of the peak value, and operate in the linear range of the FBG spectrum slope [30] [31]. The experimental results show that FBG-based sensor is a promising tool for ultrasonic detection.

However, there are still several technical challenges that need to be overcome to improve the performance of current FBG-based ultrasonic sensors. Among them are the improvement of two key specifications, sensitivity and speed, which indicate the smallest detectable strains and the largest detectable ultrasonic frequency. The demand for high sensitivity is that the environment where ultrasonic sensors are embedded contains much noise. High detection speed indicates that the ultrasonic sensors can instantaneously capture most of the frequency components of the ultrasound. π-phase-shifted FBGs (πFBGs) are a special type of FBGs whose reflection spectrum features a notch in the center of the grating caused by a π-phase discon-

tinuity [32] [33], and draw a great deal of attention for high sensitivity ultrasonic detection [34][35][36]. The πFBG can be conceptually considered as a Fabry-Perot cavity formed by two FBG mirrors because of the phase discontinuity. When the two mirrors are highly reflective, the quality factor of the Fabry-Perot cavity is increased, resulting in an extremely narrow spectral notch for highly sensitive ultrasonic sensing. Although a few experiments of ultrasonic detection based on πFBGs have been reported, the response of πFBG under ultrasonic waves has not been fully understood. This thesis aims to simulate the responses of πFBGs when impinged by ultrasonic pressure waves and provide guidance to design and optimize πFBG-based ultrasonic sensors.

1.2 Thesis Organization

This thesis is organized as follows: Chapter 1 provides the background and the motivation of the research on fiber optic ultrasonic detection. Chapter 2 introduces the effects on the optical fiber and fiber grating area of the ultrasonic pressure waves impinging onto fibers. A model of fiber grating and ultrasonic waves are established. We also discuss the necessary couple mode theory and transfer matrix method for simulating the FBG spectrum in this chapter. Chapter 3 presents the implementation of numerical simulation using Matlab, and analyzes the wavelength sensitivity change of uniform FBGs. In chapter 4, the results on wavelength sensitivity, intensity sensitivity as well as directivity of πFBGs for different designs are given. We also compares the performance of uniform FBGs and πFBGs. Chapter 5 discusses the grating pitch change and the refractive index change caused by longitudinal and shear ultrasonic waves, and compares the results of ultrasonic longitudinal waves and shear waves on the performance of πFBGs. Chapter 6 provides several conclusions of

the thesis.

Chapter 2

Modeling and Methods

The goal of this chapter is to establish a mathematical model of ultrasonic pressure waves, and introduce an efficient numerical method to simulate the response of FBGs when impinged by ultrasonic pressure waves. In addition, the changes related to parameters of fiber gratings caused by ultrasound will be detailed.

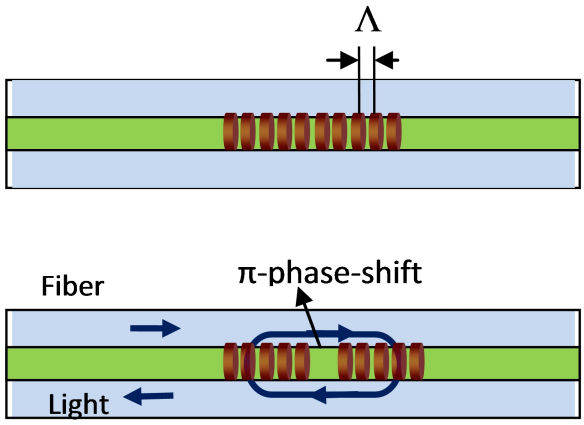

Figure 2.1: Schematics of a uniform FBG (upper graph) and a πFBG(lower graph).

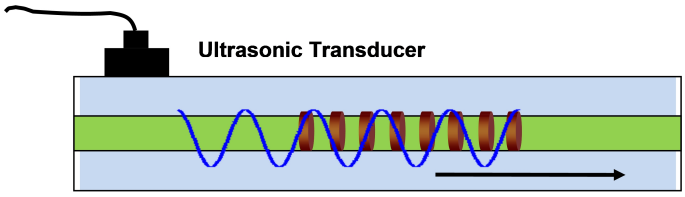

Figure 2.2: Schematic of a ultrasonic wave propagating in the optical fiber

2.1 Influence of Ultrasonic Waves on Fiber Bragg Gratings

The schematic of a uniform FBG and a πFBG is shown in Fig. 2.1. A uniform FBG, which consists of periodic refractive index modulation in the fiber core along the fiber axis, can be seen as a distributed Bragg reflector. Once the Bragg condition is satisfied, the forward propagating light is reflected at a wavelength called Bragg wavelength (λ_B): [37]

$$\lambda_B = 2n\Lambda \tag{2.1}$$

where λ_B is Bragg wavelength, n is the effective refractive index of optical mode propagating along the fiber, and Λ is the period of the FBG structure.

The πFBG is a type of nonuniform FBG, which consists of a phase jump of π at the center of the grating. The phase jump divides the grating into two parts of uniform FBGs and results in a deep notch at the center of the reflection spectrum.

When the FBG is impinged by ultrasonic waves, the mechanical strain will have an influence on the optical fiber and the FBG in several ways, causing the Bragg wavelength shifts. Those influences will be discussed in the following sections. We consider the case of ultrasonic pressure wave that propagates along the fiber axis, as shown in Fig. 2.2.

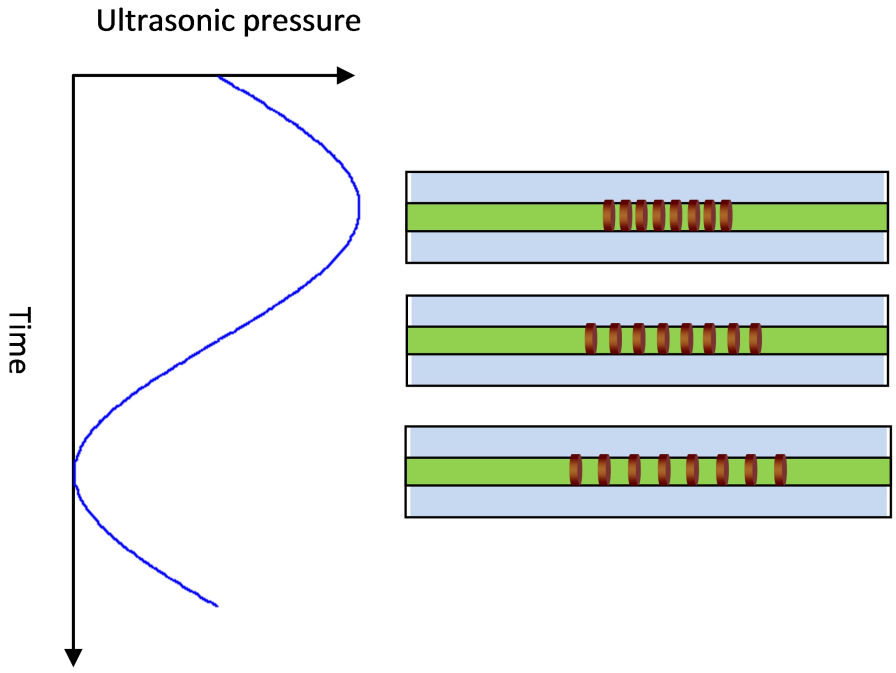

Figure 2.3: Illustration of the ultraosnic-induced geometric effect on uniform FBG

2.1.1 Geometric Effect

We start with the phase of the light propagating through the fiber grating, which can be expressed as $\phi = \beta L$. L is the length of the fiber, and β is the propagation constant of light. The mechanical strain-induced phase shift at the output is [38]

$$\Delta\phi = \beta\Delta L + L\Delta\beta \tag{2.2}$$

The first term in the right hand side of Eq. 2.2 indicates the changes in physical length of the fiber. In the case of a fiber grating region, it denotes the grating pitch changes caused by the ultrasonic waves. This direct effect is called ultrasonic-induced geometric effect, as illustrated in Fig. 2.3. For a given ultrasonic pressure P, the stress

can be written as

$$\sigma = \begin{bmatrix} -P \\ -P \\ -P \end{bmatrix} \tag{2.3}$$

In an elastic and isotropic material, such as optical fiber, the strain is related to stress by

$$\begin{bmatrix} \epsilon_{xx} \\ \epsilon_{yy} \\ \epsilon_{zz} \\ \epsilon_{xy} \\ \epsilon_{yz} \\ \epsilon_{zx} \end{bmatrix} = \begin{bmatrix} \frac{1}{E} & -\frac{\nu}{E} & -\frac{\nu}{E} & 0 & 0 & 0 \\ -\frac{\nu}{E} & \frac{1}{E} & -\frac{\nu}{E} & 0 & 0 & 0 \\ -\frac{\nu}{E} & -\frac{\nu}{E} & \frac{1}{E} & 0 & 0 & 0 \\ 0 & 0 & 0 & \frac{1}{G} & 0 & 0 \\ 0 & 0 & 0 & 0 & \frac{1}{G} & 0 \\ 0 & 0 & 0 & 0 & 0 & \frac{1}{G} \end{bmatrix} \begin{bmatrix} \sigma_{xx} \\ \sigma_{yy} \\ \sigma_{zz} \\ \tau_{xy} \\ \tau_{yz} \\ \tau_{zx} \end{bmatrix} \tag{2.4}$$

For a ultrasonic pressure wave which has no shear components, the strain vector of optical fiber caused by the pressure wave can be written as [38]

$$\begin{bmatrix} \epsilon_{xx} \\ \epsilon_{yy} \\ \epsilon_{zz} \end{bmatrix} = \begin{bmatrix} -\frac{1-2\nu}{E}P \\ -\frac{1-2\nu}{E}P \\ -\frac{1-2\nu}{E}P \end{bmatrix} \tag{2.5}$$

ϵ_{zz} in Eq. 5.3 represents the strain in the direction of fiber axis. Thus, the geometric effect can be quantitatively written as [38]

$$\beta \Delta L = \beta \epsilon_{zz} L = -\frac{\beta(1-2\nu)LP}{E} \tag{2.6}$$

where E is the Young's modulus of the fiber, and ν is Poisson's ratio.

2.1.2 Elasto-optic Effect

In addition to geometric effect, ultrasonic strain leads to other changes to the optical fiber and fiber grating according to the second term of Eq. 2.2. Due to the change of propagation constant β, the second term can be broken down into two terms [38]:

$$L\Delta\beta = L\frac{d\beta}{dn}\Delta n + L\frac{d\beta}{dD}\Delta D \tag{2.7}$$

where D represents the diameter of the fiber. The first term of Eq. 2.7 takes the refractive index change caused by ultrasonic waves into account, and thus is called elasto-optic effect or strain-optic effect. It is known $\beta = n_{eff}k_0$. Because $n_{cladding} < n_{eff} < n_{core}$ and the difference between $n_{cladding}$ and n_{core} is very small, we have $d\beta/dn = k_0$. In the rest of the thesis we use n to denote the effective refractive index. The second term of Eq. 2.7 is called waveguide mode dispersion effect due to the change in fiber diameter produced by the ultrasonic-induced strain. It is worth noting that this waveguide mode dispersion effect is negligible compared with the other two effects.

From the elasto-optic effect, the change in optical indicatrix is given by [38]

$$\Delta(\frac{1}{n^2})_i = \sum_{j=1}^{6} p_{ij}\epsilon_j \tag{2.8}$$

Because the ultrasonic wave propagates longitudinally along the fiber axis, the shear strain elements $\epsilon_4 = \epsilon_5 = \epsilon_6 = 0$. The strain-optic tensor for a homogeneous isotropic

material can be simplified to [38]

$$P_{ij} = \begin{bmatrix} p_{11} & p_{12} & p_{12} \\ p_{12} & p_{11} & p_{12} \\ p_{12} & p_{12} & p_{11} \end{bmatrix} \tag{2.9}$$

where p_{11} and p_{12} are the components of strain-optic tensor of the optical fiber material.

$$\Delta(\frac{1}{n^2})_{x,y,z} = -\frac{p_{11}P(1-2\nu)}{E} - \frac{2p_{12}P(1-2\nu)}{E} \tag{2.10}$$

$$= -\frac{P(1-2\nu)}{E}(p_{11}+2p_{12}) \tag{2.11}$$

Therefore, the change of the refractive index is

$$\Delta n_x = \Delta n_y = \Delta n_z = \Delta n = \frac{n^3 P}{2E}(1-2\nu)(p_{11}+2p_{12}) \tag{2.12}$$

2.1.3 Spectral Response of FBG Under Pressure Waves

From Eq. 2.1 Bragg wavelength of a FBG shifts when either the grating length or the refractive index changes. The wavelength shift is also used to demodulate the pressure caused by ultrasonic strain. According to Eq. 2.1, for a pressure change of ΔP, the wavelength shift $\Delta\lambda_{BP}$ is given by [39]

$$\frac{\Delta\lambda_{BP}}{\lambda_{BP}} = \frac{\Delta(n\Lambda)}{n\Lambda} = \left(\frac{1}{\Lambda}\frac{\partial\Lambda}{\partial P} + \frac{1}{n}\frac{\partial n}{\partial P}\right)\Delta P \tag{2.13}$$

We have discussed the change of fiber length and the change of refractive index due to the geometric effect and elaso-optic effect, as shown in Eq. 2.6 and Eq. 2.12. Considering the change of grating period is exactly the same as that of optical fiber

length, the normalized pitch-pressure and the index-pressure coefficients are given by

$$\frac{\Delta\Lambda}{\Lambda} = \frac{\Delta L}{L} = -\frac{(1-2\nu)\Delta P}{E} \tag{2.14}$$

$$\frac{\Delta n}{n} = \frac{n^2\Delta P}{2E}(1-2\nu)(2p_{12}+p_{11}) \tag{2.15}$$

Substituting Eq. 2.14 and Eq. 2.15 into Eq. 2.13, the spectral shift of the FBG with respect to the ultrasonic-induced pressure can be expressed by [39]

$$\Delta\lambda_{BP} = \lambda\left[-\frac{(1-2\nu)}{E} + \frac{n^2}{2E}(1-2\nu)(2p_{12}+p_{11})\right]\Delta P \tag{2.16}$$

It shows in Eq. 2.16 that the wavelength shift is directly proportional to the pressure change ΔP.

2.1.4 Model of Ultrasonic Waves

In solid materials the ultrasonic waves can travel in the forms of longitudinal waves, shear waves, surface waves and plate waves, based on the way particles oscillate [40]. Fig. 2.4 illustrates the difference of the longitudinal ultrasonic wave and shear ultrasonic wave. Ultrasonic pressure waves, which can yield equal amount of strain in any direction, can be seen as a series of expansions and compressions along the fiber axis. Therefore, the time-dependent ultrasonic pressure wave can be modeled by [2]

$$\Delta P(z,t) = \Delta P_0 \cos(\frac{2\pi}{\lambda_s}z - \omega t) \tag{2.17}$$

where ΔP_0, λ_s, ω, are the peak pressure, the wavelength of ultrasonic wave in the optical fiber, and the angular frequency, respectively; z is the coordinate along the fiber axis direction; and t is the time. The sinusoidal model given by Eq. 2.17 is valid

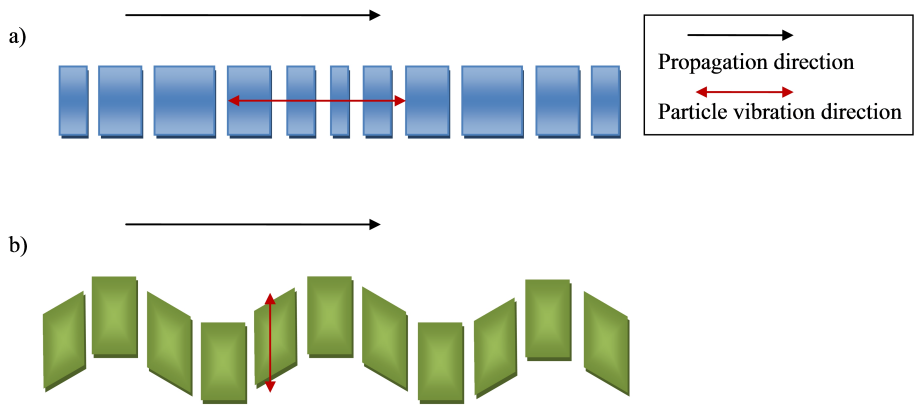

Figure 2.4: Illustration of a)longitudinal wave and b) shear wave

for both high frequency waves and low frequency waves. For low-frequency ultrasonic modulation, the strain is often simplified as a constant over the FBG length, if the wavelength of ultrasonic wave is far greater than the length of FBG. However, when the wavelength of ultrasonic wave is comparable or shorter than the length of fiber grating, the perturbation cannot be regarded as uniform and constant. Hence, the numerical approach has to be used to analyze the response of fiber gratings under non-uniform tensile and compressive strains, as is discussed in the rest of this chapter.

2.2 Models of Fiber Bragg Gratings

2.2.1 Coupled Mode Theory and Uniform FBGs

The coupled mode theory is a powerful mathematical tool to analyze the wave propagation and interactions with materials in optical waveguide. Coupled mode theory consider the grating structure as the perturbation to an optical waveguide [41]. Coupling of guided modes occurs due to the perturbation. A number of fiber grating

structures have been successfully modeled based on coupled mode theory, and the simulation results show excellent matches with experiment results.

For uniform FBGs, there exist closed-form solutions of coupling mode equations. Before starting solving these coupled mode equations, we introduce the perturbation to effective refractive index $\delta n(z)$: [37]

$$\delta n(z) = \overline{\delta n}\{1 + \nu \cos[\frac{2\pi}{\Lambda} z + \phi(z)]\} \tag{2.18}$$

where $\delta n(z)$ is the "dc" index change, ν is the fringe visibility of the index change, Λ is the grating period and $\phi(z)$ denotes the grating chirp. For single mode FBG, the simplified coupled mode equations can be expressed [37]

$$\frac{dR}{dz} = i\hat{\sigma}R(z) + i\kappa S(z) \tag{2.19}$$

$$\frac{dS}{dz} = -i\hat{\sigma}S(z) - i\kappa^* R(z) \tag{2.20}$$

where $R(z) = A(z)\exp(i\delta z - \phi/2)$ and $S(z) = B(z)\exp(-i\delta z + \phi/2)$ are the amplitudes of forward-propagating mode and backward-propagating mode. In these equations, κ is "ac" coupling, and $\hat{\sigma}$ is the general "dc" coupling coefficient. They are defined as [37]

$$\hat{\sigma} = \delta + \sigma - \frac{1}{2}\frac{d\phi}{dz} \tag{2.21}$$

$$\kappa = \kappa^* = \frac{\pi}{\lambda}\nu\overline{\delta n} \tag{2.22}$$

The detuning δ and σ in Eqs. 2.21 and 2.22 are defined as [37]

$$\delta = \beta - \frac{\pi}{\Lambda} = 2\pi n(\frac{1}{\lambda} - \frac{1}{\lambda_D}) \tag{2.23}$$

$$\sigma = \frac{2\pi}{\lambda}\overline{\delta n} \tag{2.24}$$

For uniform FBG, in which case the "dc" refractive index change $\overline{\delta n}$ is a constant and the grating chirp $d\phi/dz = 0$, κ, σ, $\hat{\sigma}$ in Eqs. 2.22, 2.2.1, 2.21 are constants. By applying the boundary conditions $R(-L/2) = 1$,$S(L/2) = 0$, we obtain the analytical expression of power reflection [37]:

$$r = \frac{-\kappa \sinh^2(\sqrt{\kappa^2 - \sigma^2}L)}{\cosh^2(\sqrt{\kappa^2 - \sigma^2}L) - \frac{\hat{\sigma}^2}{\kappa^2}} \tag{2.25}$$

2.2.2 Non-uniform FBGs and Transfer Matrix Method

In this part, we consider the modeling of non-uniform FBGs, especially the πFBG. Two approaches to modeling non-uniform FBGs are introduced and compared. We also demonstrate the use of Transfer Matrix Method in the numerical simulation of spectral response of πFBG.

Despite of the fact that uniform FBGs have been vastly investigated and utilized, the non-uniform FBGs, such as apodized FBGs, chirped FBGs, and phase-shift FBGs, have numerous unique benefits and find many practical applications. However, it is hard to find closed-form solutions for these equations like Eq. 2.25 due to the designed non-uniform refractive index modulation. Therefore, numerical methods have to be used to calculate the reflection spectra. Direct-integration approach and piecewise-uniform approach are two standard approaches.

The direct-integration approach directly solves the coupled mode equations of non-uniform gratings by resorting to numerical integration, for example, Runge-Kutta numerical integration [37]. This method is straightforward, but is usually not a fast method. On the contrary, the piecewise-uniform approach is fast, easy to implement,

and accurate enough. This method is to divide a non-uniform grating into multiple uniform pieces, and multiply the analytical solutions of each uniform piece. As the analytical solutions in each uniform section are expressed in a form of a 2×2 matrix, this approach is also called Transfer Matrix Method (T-Matrix Method) [37].

To model πFBG by Transfer Matrix Method, the fiber grating with length of L is divided into M sections. Usually the larger the number M is, the more accurate this approach is, but it is worth noting that M cannot be arbitrarily large, as the solution of coupled mode equations (Eq. 2.25)is not valid for the uniform grating with only a few period long. The amplitudes of forward-propagating mode and backward-propagating mode before and after the i^{th} uniform section are expressed in a matrix F_i such as [37]:

$$\begin{bmatrix} R_i \\ S_i \end{bmatrix} = \mathbf{F_i} \begin{bmatrix} R_{i-1} \\ S_{i-1} \end{bmatrix} = \begin{bmatrix} F_{11} & F_{12} \\ F_{21} & F_{22} \end{bmatrix} \begin{bmatrix} R_{i-1} \\ S_{i-1} \end{bmatrix} \tag{2.26}$$

where R_i, S_i are the forward-propagating mode and backward-propagating mode after the i^{th} uniform section, while R_{i-1}, S_{i-1} represent the forward-propagating mode and backward-propagating mode before the i^{th} uniform section. The elements in matrix F_i are defined by [37]

$$F_{11} = F_{22}^* = \cosh(\gamma_B \Delta z) - i\frac{\hat{\sigma}}{\gamma_B}\sinh(\gamma_B \Delta z) \tag{2.27}$$

$$F_{12} = F_{21}^* = -i\frac{\kappa}{\gamma_B}\sinh(\gamma_B \Delta z) \tag{2.28}$$

where "*" represents the complex conjugate, Δz is the length of the i^{th} uniform section, and $\gamma_B = \sqrt{\kappa^2 - \hat{\sigma}^2}$, where κ and $\hat{\sigma}$ are the same as we discussed in Eqs. 2.21 and 2.22. The output amplitude are obtained by multiplying all the matrices for

individual sections such as

$$\begin{bmatrix} R_M \\ S_M \end{bmatrix} = \mathbf{F} \begin{bmatrix} R_0 \\ S_0 \end{bmatrix} \tag{2.29}$$

where $\mathbf{F} = \mathbf{F_M} \cdot \mathbf{F_{M-1}} \cdots \mathbf{F_1}$. To take phase shift into account, we insert a phase-shift matrix at the position of the phase shift such as [37]

$$\mathbf{F_\Phi} = \begin{bmatrix} \exp\left(\frac{-i\phi_i}{2}\right) & 0 \\ 0 & \exp\left(\frac{i\phi_i}{2}\right) \end{bmatrix} \tag{2.30}$$

where ϕ_i represents the shift of the phase. For a π-phase shift, Eq. 2.30 can be written as

$$\mathbf{F}_\pi = \begin{bmatrix} -i & 0 \\ 0 & i \end{bmatrix} \tag{2.31}$$

The output amplitudes through the entire non-uniform FBG are obtained by applying the boundary conditions, $R_0 = R(L) = 1$, and $S_0 = S(L) = 0$. Therefore, the amplitude reflection coefficient $\rho = R_M/S_M$, and power reflection coefficient $r = |\rho|^2$ are calculated by T-Matrix Method.

Chapter 3

Numerical Analysis of Uniform Fiber Bragg Gratings

3.1 Overview

Now we have the preliminary knowledge for implementing the simulation of the spectral response of uniform FBG impinged by ultrasonic pressure waves. We first describe the implementation using Matlab. The numerical simulation results of wavelength shifts caused by ultrasonic waves are shown. Since the length and refractive index modification depth of a uniform FBG are the two key parameters for designing FBG-based fiber ultrasonic sensors, we discuss in detail the wavelength sensitivity with respect to the ratio between grating length and ultrasonic wavelength, when these two parameters change.

3.1.1 Simulation Implementation

To simulate the spectral response of a uniform FBG, we first need to obtain the reflection spectrum simply by applying Eq. 2.25. The necessary parameters of the

n_{eff}	1.4453
λ_D	1550 nm
δn_0	1×10^{-4}
L	10 mm
M	100

Table 3.1: Parameters of uniform fiber Bragg grating in the simulation

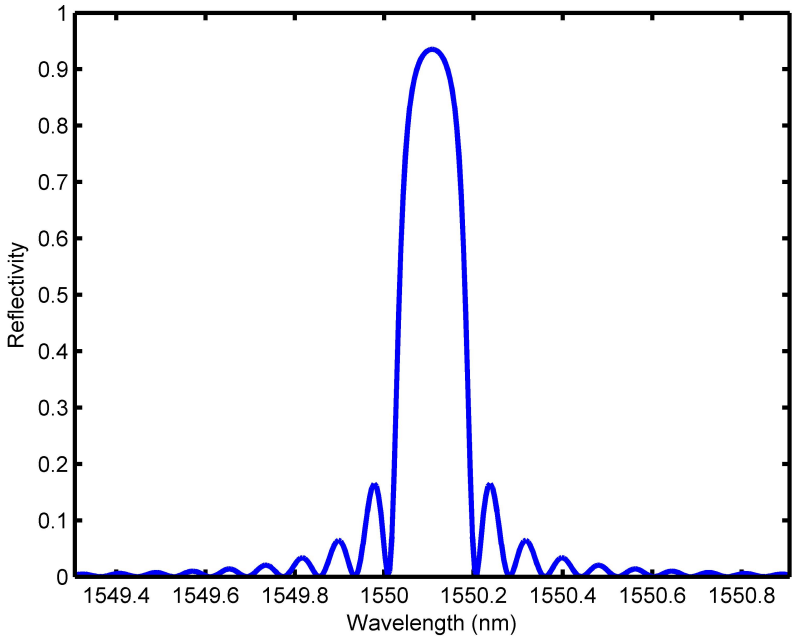

Figure 3.1: Reflection spectrum of uniform FBG

uniform FBG used for simulation are listed in table 3.1, and the result is plotted in Fig. 3.1. Note that the maximal reflectivity does not occur at the designed wavelength λ_D, which is 1550 nm. This is because the designed wavelength $\lambda_D = 2n\Lambda$ is valid for Bragg scattering by infinitesimally weak grating with a period Λ, which corresponds to δn approaches 0. In reality, the Bragg wavelength of grating is typically greater than the designed wavelength, for δn_{eff} is larger than 0 [37].

It is known that the fiber grating pitch and refractive index are affected by

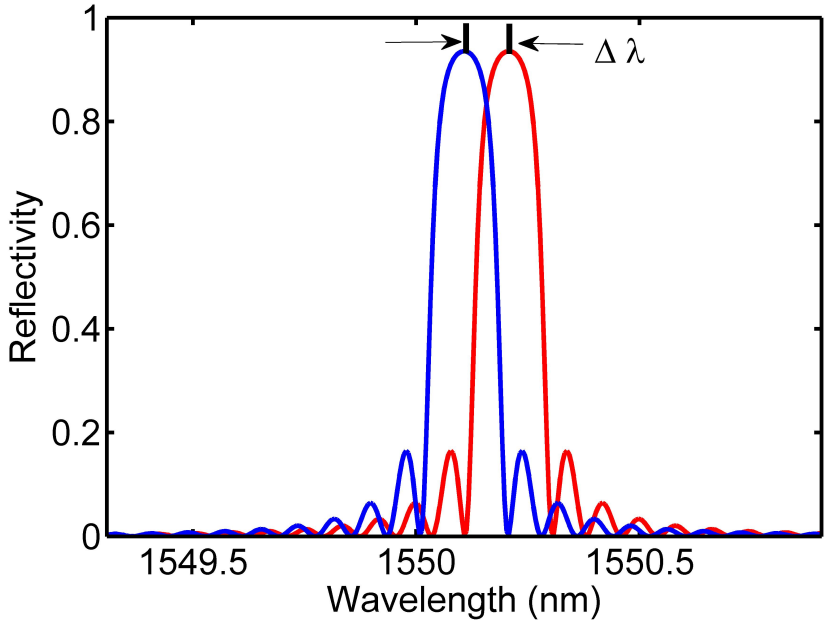

Figure 3.2: The wavelength shift caused by ultrasonic strain

ultrasonic-induced strain according to geometry effect and elasto-optic effect. We can obtain the new grating pitch and refractive index by adding the variation such as

$$\Lambda' = \Lambda + \Delta\Lambda \tag{3.1}$$

$$\overline{\delta n'} = \overline{\delta n} + \Delta n \tag{3.2}$$

where $\Delta\Lambda$ and Δn are modulated by ultrasonic-induced pressure ΔP, as discussed in Eq. 2.14 and Eq. 2.15. Thus, the perturbation to the effective index when ultrasonic wave is induced becomes:

$$\delta n' = \overline{\delta n'} + \nu\overline{\delta n}\cos\left[\frac{2\pi}{\Lambda'}z + \phi(z)\right] \tag{3.3}$$

Substituting Eq. 3.3 into the program that we calculate the reflection spectrum, we

Symbol	Physical Quantity	Value	Unit
E	Young's modulus of optical fiber	70	GPa
ν	Poisson's ratio	0.17	-
p_{11}	1,1 element in strain-optic tensor	0.121	-
p_{12}	1,2 element in strain-optic tensor	0.270	-
s	ultrasound velocity in fused silica	4000	m/s
P	Peak pressure amplitude of ultrasonic wave	1	MPa

Table 3.2: Parameters of the ultrasonic wave and optical fiber used in the simulation

can have the wavelength shift at a given ultrasonic frequency, as shown in Fig. 3.2. As time-varying ultrasonic waves produce time-dependent wavelength shift, we define the wavelength sensitivity as the peak Bragg wavelength shift caused by ultrasonic wave with unit pressure amplitude. In our simulation, the relevant parameters of ultrasonic waves and the optical fiber are listed in table 3.2.

3.2 Wavelength Sensitivity and Grating Length

Fig. 3.3 plots the result of wavelength sensitivity with respect to ultrasonic frequency when the length of uniform FBGs changes from 8 mm to 14 mm. The graph in logarithmic scale is given in Fig. 3.4. The refractive index modulation depth is set to 1×10^{-4} in the simulation, and the peak pressure amplitude of ultrasonic wave is 1 MPa. The wavelength sensitivity of all of these FBGs starts from the same maximum of 4.5 pm/MPa when the ultrasonic frequency is zero. As the ultrasonic frequency increases, the wavelength sensitivity of all the uniform FBGs decreases, and reaches their first minimum which is almost zero. The wavelength sensitivity of uniform FBG with longer length drops more quickly to the first local minimum, which means that FBGs with shorter length offers better wavelength sensitivity than those with longer grating length. This is because the average change to the refractive index and

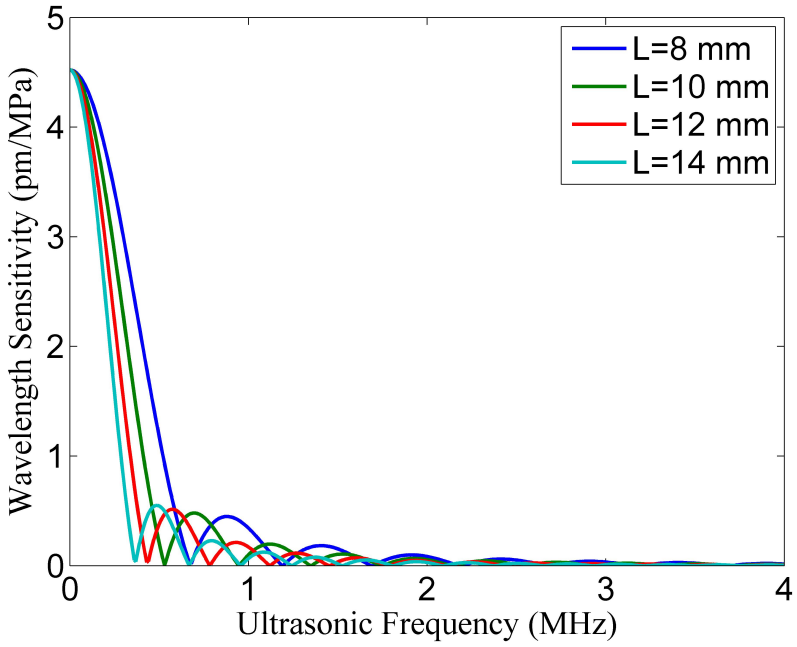

Figure 3.3: Wavelength sensitivity of uniform FBG with $\delta n_0 = 1 \times 10^{-4}$ as a function of ultrasonic frequency in linear scale.

the grating period length caused by ultrasonic waves decreases when the ultrasonic frequency increases. After the first local minimum, the sidelobes appear at the tail of the curves as the ultrasonic frequency continues to increase. It is worth noting that the wavelength sensitivity becomes very weak when the ultrasonic frequency is higher than 3 MHz. This is due to the ultrasonic wave with multiple periods neutralizes the change of refractive index and that of the grating period length.

3.3 Wavelength Sensitivity and Refractive Index Modulation Depth

Fig. 3.5 shows the wavelength sensitivity of uniform FBGs with length of 10 mm as a function of ultrasonic frequency when the refractive index modulation depth changes

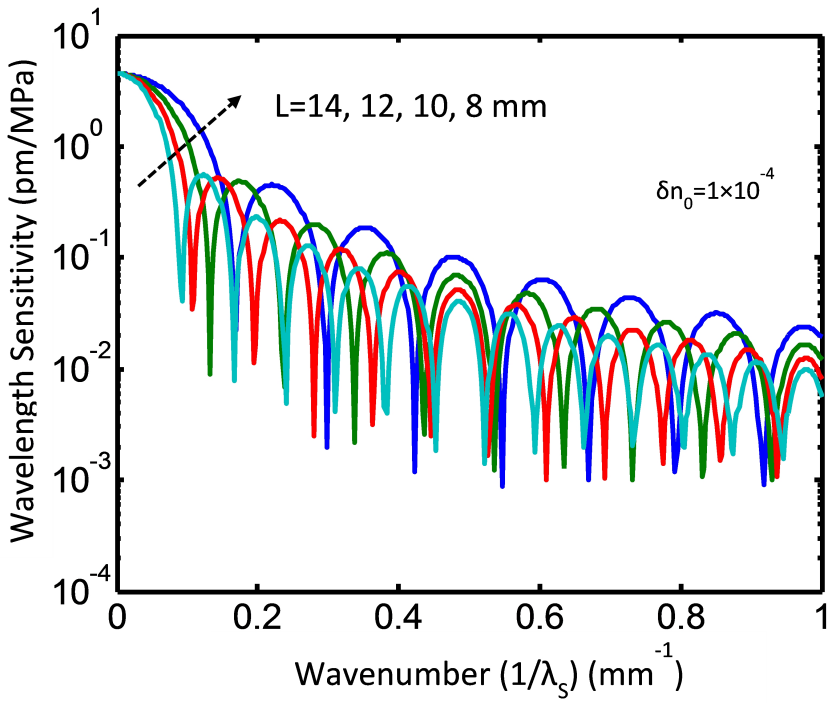

Figure 3.4: Wavelength sensitivity of uniform FBG with $\delta n_0 = 1 \times 10^{-4}$ as a function of ultrasonic wavenumber in logarithmic scale.

from 6×10^{-5} to 1.2×10^{-4}. The graph in logarithmic scale is given in Fig. 3.6. Like the curves in Fig. 3.3, the wavelength sensitivity drops as the ultrasonic frequency increases in the low frequency region, and the sidelobe structure occurs in the high frequency region. However, curves of different refractive indices almost overlap in the entire frequency region except for their first sidelobes, and the wavelength sensitivity of FBGs with different refractive indices reaches every local minimum at the same ultrasonic frequency. This means that changing the refractive index modulation depth of a uniform FBG with given length does not affect the wavelength sensitivity at any ultrasonic frequency.

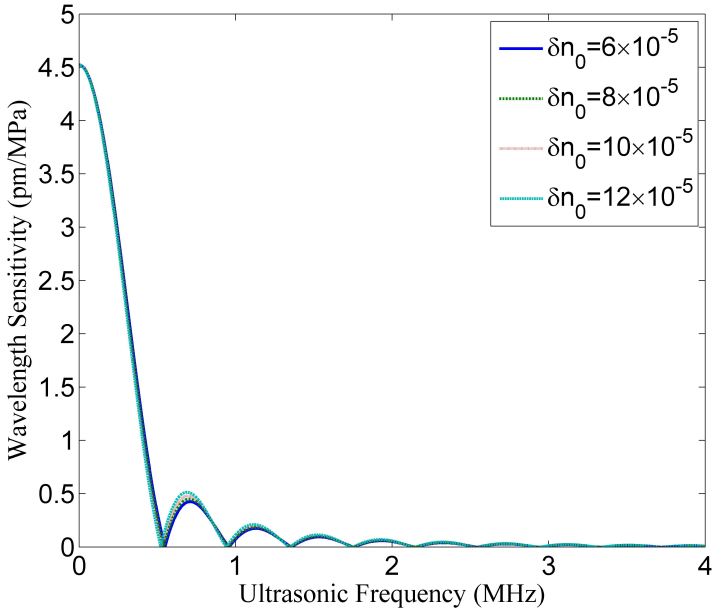

Figure 3.5: Wavelength sensitivity of uniform FBG with length of 10 mm as a function of ultrasonic frequency.

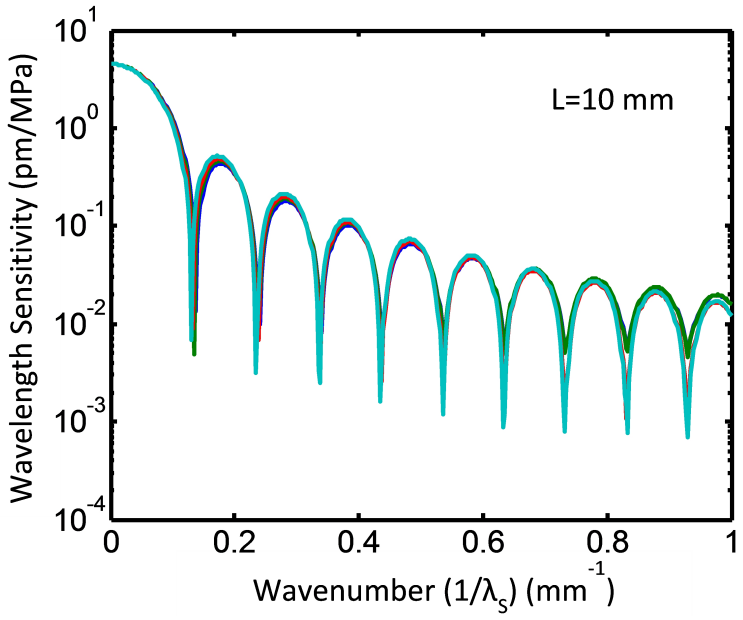

Figure 3.6: Wavelength sensitivity of uniform FBG with length of 10 mm as a function of ultrasonic wavenumber in logarithmic scale.

3.4 Conclusion

In this chapter, we elaborated the implementation of the simulation based on the model discussed in last chapter. In addition, the parameters used in the numerical simulation were discussed and the values of those parameters were given. Also, we analyzed the wavelength sensitivity of uniform FBGs with respect to grating length and refractive index modification depth. The results show that the wavelength sensitivity decreases as the ultrasonic frequency increases. Reducing the grating length can enhance the wavelength sensitivity of a uniform FBG ultrasonic sensor. Changing the refractive index modification depth, nevertheless, has little impact on the wavelength sensitivity.

Chapter 4

Numerical Analysis of π-phase-shift Fiber Bragg Gratings

4.1 Overview

πFBGs feature a deep notch at their center wavelength, and hence have a narrow bandwidth of reflection spectrum. This makes πFBGs an ideal candidate for the applications in high-sensitivity, distributed optical fiber sensing. Yet, the πFBG-based optical fiber sensors have not been fully studied for ultrasonic detection. In this chapter, besides the wavelength sensitivity, we also study another important parameter of a πFBG ultrasonic sensor named intensity sensitivity. We will investigate the performances of πFBG by changing the grating length, refractive index modification depth, and the incidence angles of ultrasonic waves impinging onto the fiber grating. In addition, the comparison of uniform FBGs and πFBGs used for ultrasonic detection will be discussed.

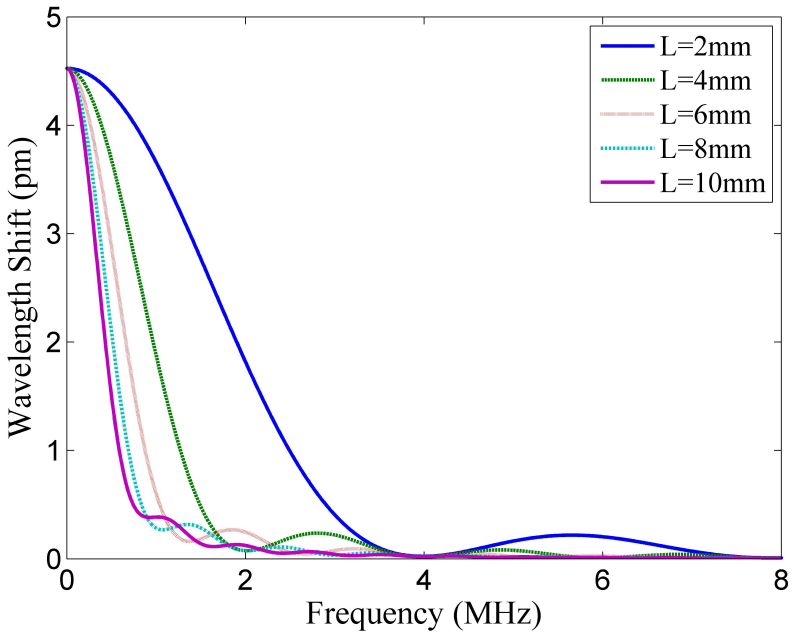

Figure 4.1: Wavelength shift of πFBG with $\delta n_0 = 1 \times 10^{-4}$.

4.2 Wavelength Sensitivity

4.2.1 Wavelength Sensitivity and Grating Length

As we find in Chapter 3 the wavelength sensitivity for πFBG is the maximum spectral shift of the πFBG Bragg wavelength caused by ultrasonic wave with unit pressure amplitude. Fig. 4.1 shows the wavelength shift with respect to ultrasonic frequency for the πFBGs with constant refractive index modulation depth $\delta n_0 = 1 \times 10^{-4}$ and grating length ranging from 2 mm to 10 mm. We assume that all the peak pressure amplitudes of ultrasonic wave are 1 MPa. The maximal wavelength shift of 4.5 pm occur when a static tensile or compressive strain applied to the grating. The wavelength shift decreases as the frequency increases, with the sidelobe structure appearing at the tail of each curves. This is due to the fact that as the ultrasonic frequency increases, the wavelength of ultrasonic wave decreases and the average net

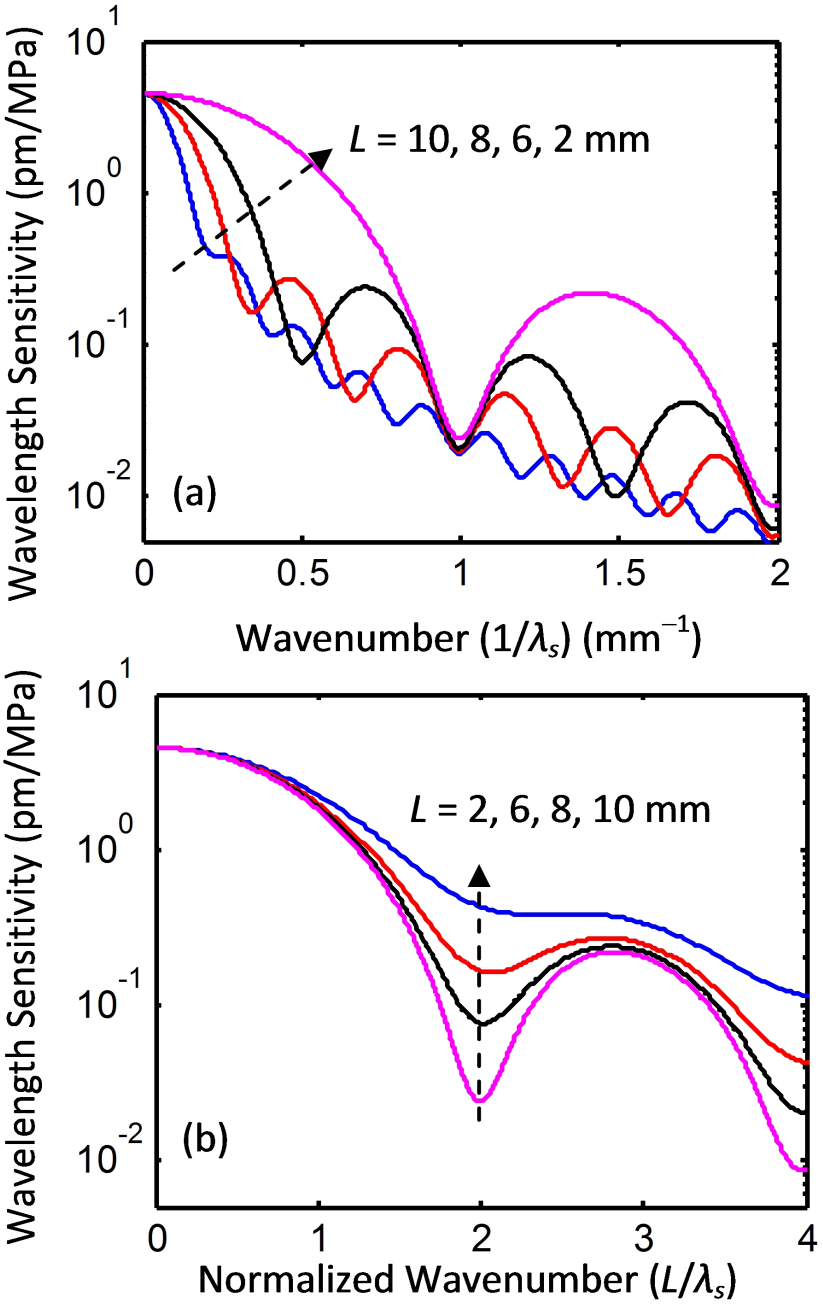

Figure 4.2: Wavelength sensitivity response of πFBG with $\delta n_0 = 1 \times 10^{-4}$. (a) Wavelength sensitivity as a function of ultrasonic wavenumber; (b) Wavelength sensitivity as a function of ultrasonic normalized wavenumber.

changes by geometric effect and elasto-optic effect over the grating decreases. In other words, the effect of stretching and compressing on fiber grating pitch cancels out each other. This "averaging effect" is more evident in Fig. 4.2 (b), which plots the wavelength sensitivity as a function of normalized ultrasonic wavenumber defined as the grating length-ultrasonic wavelength ratio (L/λ_s). It shows that when $L/\lambda_s < 2$, the wavelength sensitivities of all different lengths drop from their maximum value; at $L/\lambda_s \approx 2$, the wavelength sensitivities are around their first minimum; when $L/\lambda_s > 2$, the sidelobes occur and the wavelength sensitivities approach to their next minimum. Note that all the πFBGs fall to their first minimum at approximately the same grating length-ultrasonic wavelength ratio of $L/\lambda_s = 2$; while for unform FBGs the first minimum occurs when $L/\lambda_s = 1.3$ [42]. This exhibits that πFBGs have a larger ultrasonic bandwidth compared with uniform FBGs of the same length. The difference arises from the different spatial distributions of the light intensity along a πFBG and a uniform FBG, which will be further discussed in section 4.2.3. In the third region, the second local minimum is roughly one order of magnitude less than the first one. This indicates that the effects of tensile strain and compressive strain on fiber grating period, and the effect of the refractive index change are approximately averaged out when the ultrasonic wavelength is much smaller than the grating length.

4.2.2 Wavelength Sensitivity and Refractive Index Modulation Depth

We also carry out the simulation to investigate the effect of the refractive index modulation depth on the wavelength sensitivity of πFBGs The results are shown in Fig. 4.3, which plots wavelength sensitivity as a function of normalized ultrasonic wavenumber for πFBGs with the same length of 4 mm but with different refractive

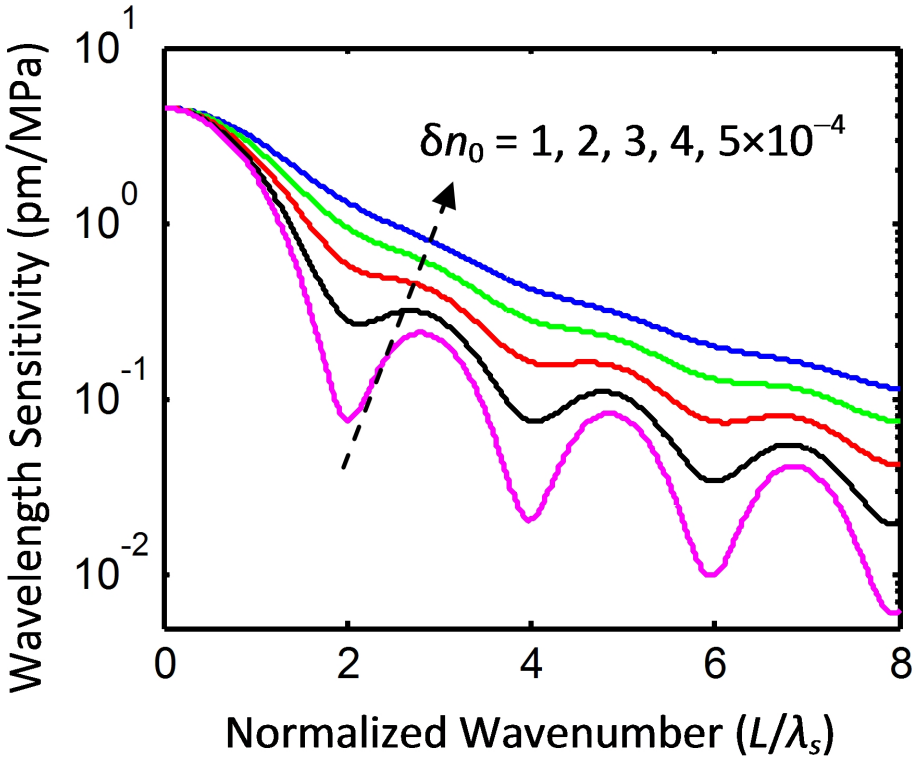

Figure 4.3: Wavelength sensitivity response of 4-mm long πFBGs of different refractive index modulation depths as a function of normalized ultrasonic wavenumber.

index modulation depth. The curves of wavelength sensitivity also start from 4.5 pm/MPa when the normalized wavenumber $L/\lambda_s = 0$, and decrease as the normalized wavenumber increases. We notice that for gratings with lower average refractive index change, the sidelobe structures still occur at the tail; while for the gratings with higher average refractive index change, the tails tend to be smooth and the sidelobe structure is less evident. Our results reveal that the gratings with higher average refractive index change achieve considerably higher wavelength sensitivity than those with lower refractive modulation depth, when impinged by the ultrasonic waves of the same frequency. For example, at frequency of 2 MHz, when the $\delta n_0 = 1 \times 10^{-4}$, the wavelength sensitivity is 0.076 pm/MPa. The wavelength sensitivity is increased

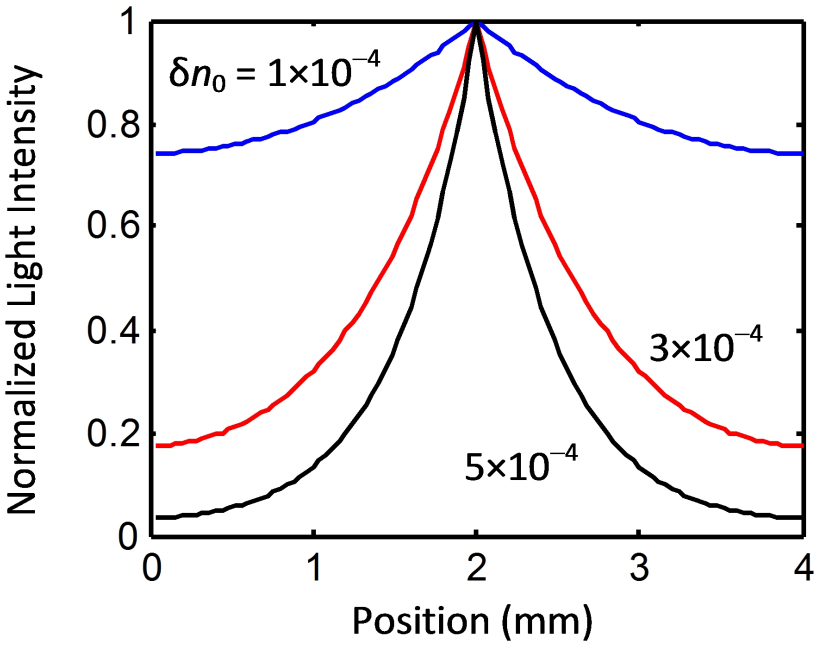

Figure 4.4: Spatial distribution of the normalized light intensity over 4-mm long πFBGs of different refractive index modulation depths.

to 0.59 pm/MPa for a δn_0 of 3×10^{-4}. The wavelength sensitivity is further increased to 1.33 pm/MPa for a δn_0 of 5×10^{-4}, which is almost 20 times better than the case for $\delta n_0 = 1 \times 10^{-4}$. The significantly enhanced wavelength sensitivity to ultrasonic waves observed in πFBGs are not present in uniform FBGs. The reason for this enhancement will be discussed in section 4.2.3. Our simulation result also indicates that fabricating strong πFBGs is an effective way to detect higher frequency ultrasonic waves, as the wavelength sensitivity is enhanced by at least one order of magnitude in the high frequency range.

4.2.3 Spatial Distribution of Light Intensity

In order to better understand the characteristics of πFBGs as mentioned earlier, the spatial distribution of light intensity over a 4 mm long πFBGs is reported in Fig. 4.4. With π phase shift at the center of the fiber grating, the light energy is more distributed around the center of πFBG, and decays from the center to the two ends. This center-intense spatial confinement phenomenon is more evident for the πFBG with larger refractive modulation depth. The reason for this phenomenon is that, as a πFBG can be considered as a Fabry-Perot cavity formed by two uniform FBG reflection mirrors, a larger refractive index modulation depth yields a higher reflectivity of each of the FBG mirrors, leading to higher cavity quality factor and a better spatial confinement of the light around the center of the πFBG and therefore reducing the "effective length" of the πFBG. The unique light energy distribution in πFBGs is also responsible for the larger ultrasonic bandwidth of a πFBG compared to a uniform FBG, as mentioned in section 4.2.1.

4.3 Intensity Sensitivity

Besides the wavelength sensitivity, we also study another parameter called intensity sensitivity, as shown in Fig. 4.5, which is defined by the amplitude of the reflectivity variations at the wavelength corresponding to 50% reflection of the πFBG reflection spectrum in presence of ultrasonic wave with unit pressure amplitude. In term of practical applications, the intensity sensitivity is more relevant, as it is the sensitivity used in the narrowband laser interrogation technique for Bragg grating response demodulation [27]. This technique employs a narrow linewidth laser working in the πFBG spectral linear range (usually locked to the 50% reflection position) to detect the reflected amplitude change that is directly related to the Bragg wavelength shift.

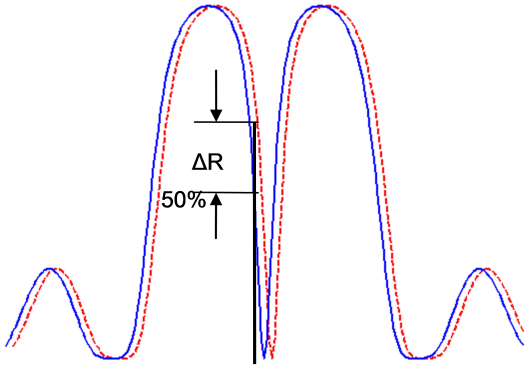

Figure 4.5: Illustration of intensity sensitivity for πFBG.

It is worth noting that the intensity sensitivity also relates to the wavelength sensitivity we discussed before through the slope of the πFBG spectral linear range such as

$$\frac{dR}{dP} = \frac{d\lambda}{dP} \cdot k \tag{4.1}$$

where dR/dP denotes the intensity sensitivity, $d\lambda/dP$ represents the wavelength sensitivity, and $k = dR/d\lambda$ is the slope of πFBG spectral linear range.

4.3.1 Intensity Sensitivity and Grating Length

Our previous analysis has revealed that a πFBG with longer length reduces the wavelength sensitivity due to the non-uniform perturbations to the refractive index and grating period. However, a longer πFBG length also reduces the bandwidth of the reflection spectral dip and increases the slope of the linear range. According to Eq. 4.1, it is worthy to study the overall effect of the πFBG length on the intensity sensitivity. The numerical results of intensity sensitivity as a function of ultrasonic wavenumber for πFBGs of different refractive index modulation depth are shown in Fig. 4.6. The intensity sensitivity decreases as the wavenumber increases. For the πFBGs with

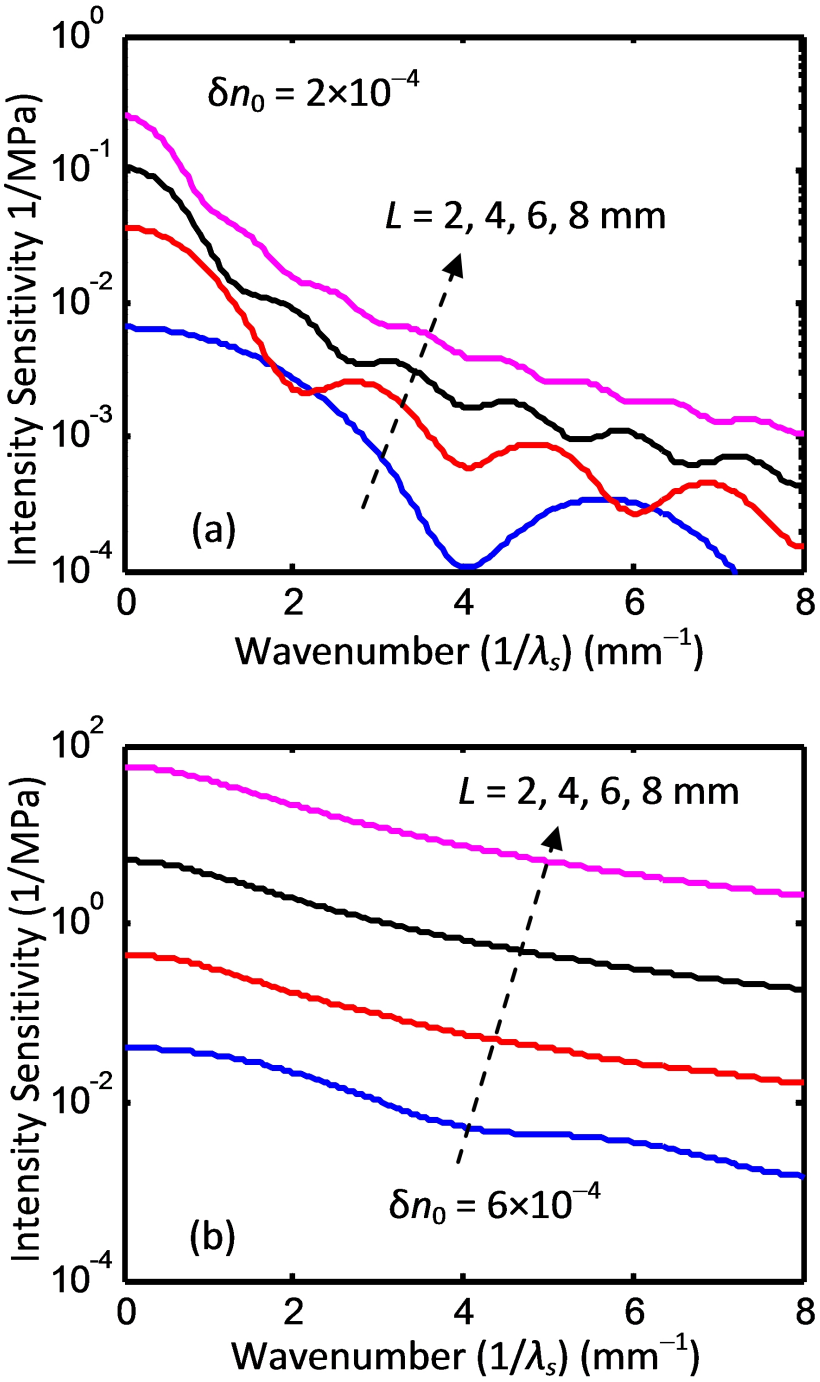

Figure 4.6: Intensity sensitivity as a function of ultrasonic wavenumber for πFBGs of different refractive index modulation depth (a) $\delta n_0 = 2\times10^{-4}$ and (b) $\delta n_0 = 6\times10^{-4}$.

both $\delta n_0 = 2 \times 10^{-4}$, we can slightly see the sidelobe structure, and that number of sidelobe is proportional to the length of πFBG; while the sidelobe structure almost disappears for the πFBGs with $\delta n_0 = 6 \times 10^{-4}$. In both cases, the intensity sensitivity of a longer πFBG is usually higher than that of a shorter one. The benefit to the intensity sensitivity of longer πFBG length is more evident in πFBGs with higher refractive index modulation depth, as shown in Fig. 4.6 (b). Therefore, increasing of πFBG length can increase the detection sensitivity of a πFBG-based ultrasonic sensor system as the increased spectral slope overcomes the reduced spectral sensitivity by a longer grating length.

4.3.2 Intensity Sensitivity and Refractive Index Modulation Depth

In addition to the effect of πFBG length change, we also investigate the effect of refractive index modulation depth on the intensity sensitivity, as shown in Fig. 4.7. The result exhibits that the intensity sensitivity increases as the refractive index modulation depth increases and it decreases as the wavenumber increases. Besides that higher refractive index modulation index can enhance the wavelength sensitivity due to the center-intense confinement phenomenon of πFBGs, higher refractive index modulation index can also narrow the spectral notch leading to a larger slope of linear region. Therefore, the intensity sensitivity, which is the product of wavelength sensitivity and the slope of linear region, can be enhanced by increasing the refractive index modulation depth.

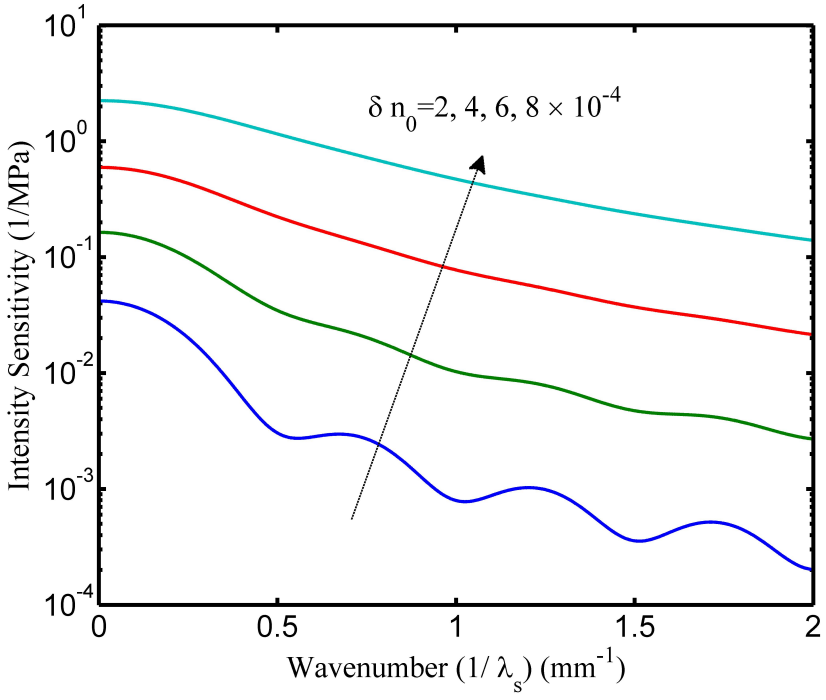

Figure 4.7: Intensity sensitivity as a function of ultrasonic wavenumber for πFBGs of 4 mm.

4.4 Comparison of Uniform FBGs and πFBGs

In this section, we compare the sensitivity performances of uniform FBGs and πFBGs for detecting pressure waves.

4.4.1 Similarities

Several numerical simulations have been performed to investigate the responses of uniform FBGs and πFBGs under ultrasonic pressure waves. We discover that for both uniform FBGs and πFBGs the wavelength sensitivity increases as the grating length decreases in the low ultrasonic frequency region.

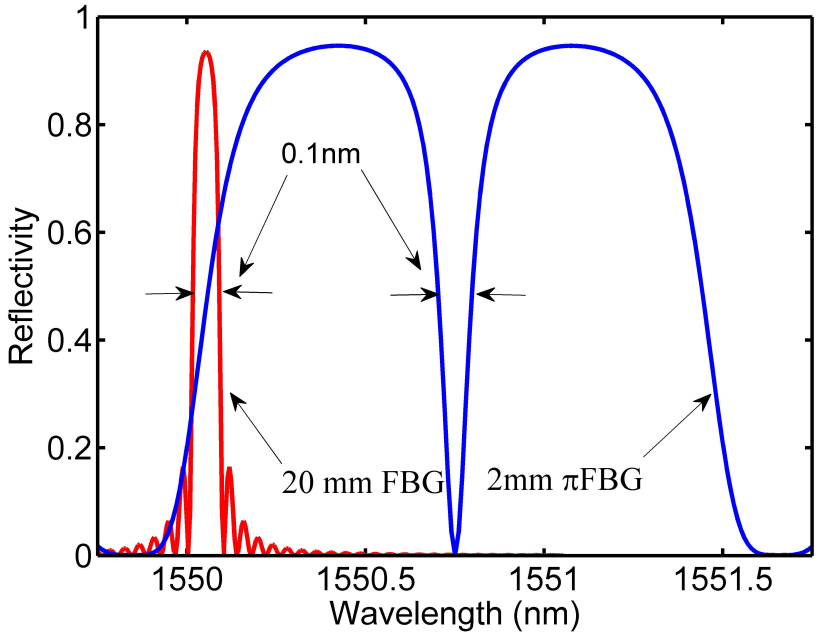

Figure 4.8: Simulated reflection spectra of a 2-mm long πFBG and a 20-mm long uniform FBG.

4.4.2 Differences

Note that the grating lengths used in the simulation for uniform FBGs and πFBGs are not in the same range. The reason is that longer grating length is required for uniform FBGs to achieve comparable reflectivity and spectral bandwidth of πFBGs with the same refractive index modulation. As shown in Fig. 4.8, the reflection spectrum of πFBG features a narrow notch, which results from the discontinuity in the center of the grating. In order to obtain the spectral bandwidth of 0.1 nm, the uniform FBG has to be made as long as 20 mm, while a 2 mm long πFBG has the same spectral bandwidth. Since shorter grating length leads to higher wavelength sensitivity, it is benefical to use πFBG to design more sensitive ultrasonic sensors.

In addition, unlike FBGs whose wavelength sensitivity does not change with different refractive index modulation depth, the wavelength sensitivity of πFBGs can be

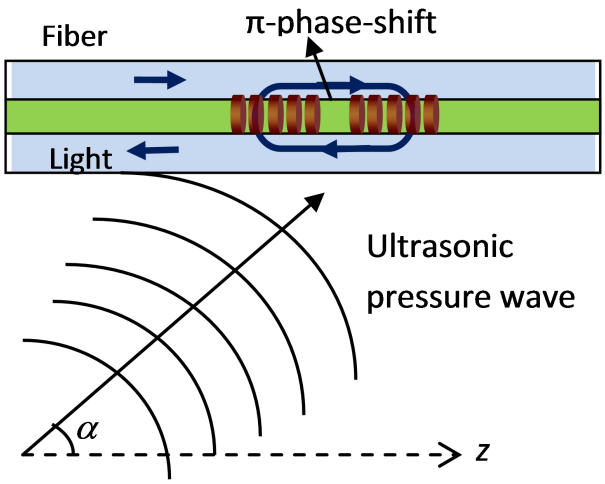

Figure 4.9: Schematic of a πFBG and an ultrasonic pressure wave impinging onto the grating with an incident angle of α

enhanced by increasing the refractive index modulation depth. As the results shown in Section 4.2.2, this enhancement is more evident in the high frequency region where usually uniform FBG ultrasonic sensors have fairly small responses. The enhancement explained in section 4.2.3 is due to the effective length reducing effect which results from the Fabry-Perot cavity formed by two uniform FBGs of a πFBG.

4.5 Directivity

Directivity is another important parameter for designing ultrasonic sensors. The results we have discussed before are based on the assumption that the pressure ultrasonic waves impinge onto the gratings from a direction parallel to the fiber axis. For pressure waves impinging onto the πFBG at an angle of α with respect to the fiber axis, as shown in Fig. 4.9, the ultrasonic length along the fiber axial direction can be

given as

$$\lambda_\alpha = \frac{\lambda_S}{|\cos\alpha|} \tag{4.2}$$

In this case the amplitude of the refractive index and the grating pitch modifications caused by ultrasonic pressure waves remain unchanged. Thus, the ratio of ultrasonic wavelength and grating length is expected to be an important factor to affect the directivity. The results of intensity sensitivity of a 4 mm πFBG with $\delta n_0 = 2 \times 10^{-4}$ with respect to incidence angle for different grating length to ultrasonic wavelength ratio are plotted in Fig. 4.10. We can clearly see that the maximum of intensity sensitivity occurs at the normal incidence. For lower L/λ_S ratio, which corresponds to lower ultrasonic frequency, the intensity sensitivity appears less directional. This is because when the ultrasonic wavelength is significantly larger than the grating length, the perturbation induced by ultrasonic waves can be considered to be uniform leading to omnidirectional response. As the ultrasonic frequency increases, the nonuniform perturbation caused by ultrasonic pressure is more sensitive to the incidence angle, and therefore the intensity sensitivity of the πFBG is highly directional. We notice that when $L/\lambda_S = 4$, the sensitivity is about 50 times higher for normal incidence ($\alpha = 90°$)than for parallel incidence. It reveals that impinging ultrasonic waves at normal incidence can enhance the intensity sensitivity for high frequency ultrasound detection. Recalling that increasing fiber length can increase the intensity sensitivity, we need to consider the tradeoff between sensitivity and directivity when designing the πFBG sensors.

Similar directivity characteristics are also observed in some other types of fiber optic sensors, such as Fabry-Perot sensors [43] and Sagnac interferometers [44]. It is worth noting that the directivity analysis is only valid for an ultrasonic wave with an isotropic stress field, such as the pressure waves. The grating ultrasonic sensor may

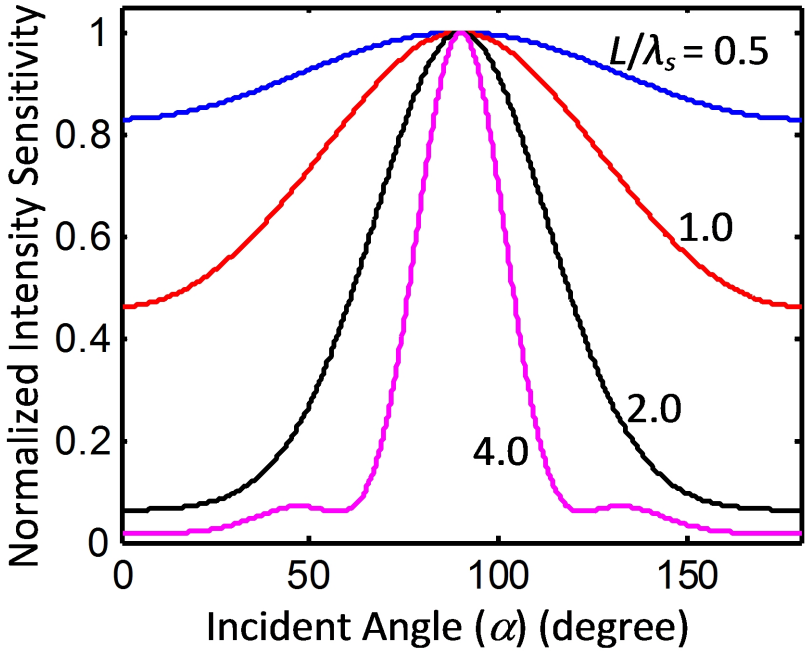

Figure 4.10: Normalized intensity sensitivity as a function of ultrasonic incident angle for 4-mm long πFBG with a refractive index modification depth $\delta n_0 = 2 \times 10^{-4}$ impinged by ultrasonic waves of different wavelength.

show completely different directivity patterns when used to detect ultrasonic waves with an anisotropic field.

4.6 Conclusion

In this chapter, we simulated the performance of πFBGs under the impact of ultrasonic pressure waves based on the model discussed in previous chapters. The results show that the wavelength sensitivity increases as the grating length decreases, and it increases as the refractive index modification depth increases. The spatial distribution of light intensity can explain the enhancement by increasing the refractive index modification depth. The intensity sensitivity increases as the grating length increases

or as the refractive index modification depth increases. In addition, the performance of uniform FBGs and πFBGs was compared to demonstrate the advantages of πFBGs to be used as a sensing element for ultrasonic detection. In the end we analyzed the directivity of a πFBG ultrasonic sensor for pressure detection. It shows that normal incidence can enhance the intensity sensitivity significantly when πFBG is used to detect high frequency ultrasonic waves.

Chapter 5

Response of πFBG Under Longitudinal or Shear Ultrasonic Waves

In Chapter 2 to Chapter 4, our simulation and discussion focus on the response of FBGs to ultrasonic pressure waves. Pressure waves are an important type of ultrasonic waves that typically exist in liquids or in the air and yield strains of the same amount in any direction on the material. However, there are ultrasonic waves of other types in solids which are more common in structural health monitoring(SHM), such as ultrasonic longitudinal waves and ultrasonic shear waves. In this chapter we will analyze the responses of πFBGs when impinged by ultrasonic longitudinal waves and shear waves. The emphasis is placed on the method of establishing new model for longitudinal or shear waves and the modification of refractive index of the fiber gratings, so that similar methods can also be applied to analyze ultrasonic waves of other types. The numerical results on the response under ultrasonic waves of those types will be compared with those under pressure waves discussed in previous

chapters.

5.1 Modification of Grating Period and Refractive Index by Longitudinal Waves

Ultrasonic longitudinal waves, whose vibration direction is parallel to the direction of propagation, have a different impact on both grating period and refractive index change from ultrasonic pressure waves. Assume the vibration direction and propagation direction are both in z direction, which is along with the fiber axis. The stress along z direction can be modeled by

$$\sigma_z = -P\cos\left(\frac{2\pi}{\lambda_s}z + \omega t\right) \tag{5.1}$$

where P is the pressure produced by the ultrasonic wave. The stress vector can be written as

$$\sigma = \begin{bmatrix} 0 \\ 0 \\ -P \end{bmatrix} \tag{5.2}$$

Recall that the strain is related to stress in Eq. 2.4 For a ultrasonic longitudinal wave which has no shear components, the strain vector of optical fiber caused by the pressure wave can be written as

$$\begin{bmatrix} \epsilon_{xx} \\ \epsilon_{yy} \\ \epsilon_{zz} \end{bmatrix} = \begin{bmatrix} \frac{\nu}{E}P \\ \frac{\nu}{E}P \\ -\frac{1}{E}P \end{bmatrix} \tag{5.3}$$

The changes in fiber grating period and fiber length are related to ϵ_{zz} by [39]

$$\frac{\Delta\Lambda}{\Lambda} = \frac{\Delta L}{L} = \epsilon_{zz} = -\frac{1}{E}P \tag{5.4}$$

We know that the interaction of ultrasonic waves and materials also causes the change of refractive index of the material, which is called elasto-optic effect or strain-optic effect. According to the elasto-optic effect discussed in 2.1.2, the change in optical indicatrix caused by an applied strain is given by [6]

$$\Delta\left(\frac{1}{n^2}\right)_i = \sum_{j=1}^{6} p_{ij}\epsilon_j \tag{5.5}$$

where p_{ij} is the strain optic tensor. For a homogeneous and isotropic fiber, the strain-optic tensor can be expressed in Eq. 2.9 The strain vector caused by the longitudinal wave is

$$\epsilon = \begin{bmatrix} \epsilon_{xx} \\ \epsilon_{yy} \\ \epsilon_{zz} \\ \epsilon_{xy} \\ \epsilon_{yz} \\ \epsilon_{zx} \end{bmatrix} = \begin{bmatrix} \frac{\nu}{E}P \\ \frac{\nu}{E}P \\ -\frac{1}{E}P \\ 0 \\ 0 \\ 0 \end{bmatrix} \tag{5.6}$$

Solve Eq. 5.5 by multiplying Eq. 2.9 and Eq. 5.6, and the change in the indicatrix is obtained as

$$\Delta\left(\frac{1}{n^2}\right)_{x,y} = [\nu p_{11} - (1-\nu)p_{12}]\frac{P}{E} \tag{5.7}$$

The refractive index related to the change in optical indicatrix is [6]

$$\begin{aligned} \Delta n_{x,y} &= -\frac{1}{2} n^3 \Delta \left(\frac{1}{n^2}\right)_{x,y} \\ &= \frac{n^3}{2E}[(1-\nu)p_{12} - \nu p_{11}]P \end{aligned} \tag{5.8}$$

Substituting Eq. 5.4 and Eq. 5.8 into Eq. 2.13, we can predict the spectral shift with respect to the ultrasonic-induced pressure by

$$\Delta\lambda_B = \lambda_B \left\{ -\frac{1}{E} + \frac{n^2}{2E}[(1-\nu)p_{12} - \nu p_{11}] \right\} \Delta P \tag{5.9}$$

5.2 Modification of Grating Period and Refractive Index by Shear Waves

As we discussed in Chapter 2, the propagation direction of shear waves is perpendicular to the direction of vibration. Assume a shear ultrasonic wave propagating along the fiber axis in z direction vibrates in x direction. The stress in x direction can be modeled by

$$\sigma_x = -P\cos\left(\frac{2\pi}{\lambda_s} z + \omega t\right) \tag{5.10}$$

where P is the pressure produced by the ultrasonic wave. The stress vector can be written as

$$\sigma = \begin{bmatrix} -P \\ 0 \\ 0 \end{bmatrix} \tag{5.11}$$

Substituting Eq. 5.11 into Eq. 2.4, the strain of optical fiber is obtained by

$$\begin{bmatrix} \epsilon_{xx} \\ \epsilon_{yy} \\ \epsilon_{zz} \end{bmatrix} = \begin{bmatrix} -\frac{1}{E}P \\ \frac{\nu}{E}P \\ \frac{\nu}{E}P \end{bmatrix} \tag{5.12}$$

The changes in fiber grating period and fiber length are related to ϵ_{zz} by [39]

$$\frac{\Delta\Lambda}{\Lambda} = \frac{\Delta L}{L} = \epsilon_{zz} = \frac{\nu}{E}P \tag{5.13}$$

Solve Eq. 5.5 using Eq. 2.9 and Eq. 5.12, the change in the indicatrix is obtained by

$$\Delta\left(\frac{1}{n^2}\right)_x = (2\nu p_{12} - p_{11})\frac{P}{E} \tag{5.14}$$

$$\Delta\left(\frac{1}{n^2}\right)_y = [\nu p_{11} - (1-\nu)p_{12}]\frac{P}{E} \tag{5.15}$$

The refractive index change can be derived from

$$\Delta n = -\frac{1}{2}n^3\Delta\left(\frac{1}{n^2}\right) \tag{5.16}$$

The components of refractive index changes are

$$\Delta n_x = \frac{n^3}{2E}(p_{11} - 2\nu p_{12})P \tag{5.17}$$

$$\Delta n_y = \frac{n^3}{2E}[(1-\nu)p_{12} - \nu p_{11}]P \tag{5.18}$$

Since the x component and y component of the refractive index change induced by shear waves are not equal, we only discuss two special cases. The first one is when a linearly polarized light whose electric field is parallel to x direction is launched into

the fiber. The second one is when a linearly polarized light whose electric field is parallel to y direction is launched into the fiber. In the first case substituting Eq. 5.13 and Eq. 5.17 into Eq. 2.13, we obtain the spectral shift with respect to the ultrasonic-induced pressure by

$$\Delta\lambda_B = \lambda_B \left[\frac{\nu}{E} + \frac{n^2}{2E}(p_{11} - 2\nu p_{12})\right] \Delta P \tag{5.19}$$

In the second case substituting Eq. 5.13 and Eq. 5.18 into Eq. 2.13, we can predict the spectral shift by

$$\Delta\lambda_B = \lambda_B \left\{\frac{\nu}{E} + \frac{n^2}{2E}\left[(1-\nu)p_{12} - \nu p_{11}\right]\right\} \Delta P \tag{5.20}$$

Since shear waves cause different refractive index changes in the x direction and y direction, the ultrasonic detection sensitivity is dependent on the polarization of the light in the fiber.

5.3 Numerical Results

The numerical simulations on intensity sensitivity of πFBGs under ultrasonic longitudinal waves and shear waves are carried out. Fig. 5.1, Fig. 5.2 and Fig. 5.3 show the results of longitudinal waves and shear waves. I need to point out that the result of shear wave is obtain based on the assumption that a linearly polarized light whose electric field is parallel to x direction or y direction is incident to the fiber. It is evident that the πFBG sensor has a higher intensity sensitivity when impinged by longitudinal waves than by shear waves. We can attribute the differences of intensity sensitivity to the different overall effect of grating period change and refractive index change caused by different types of ultrasonic waves. For longitudinal waves, under

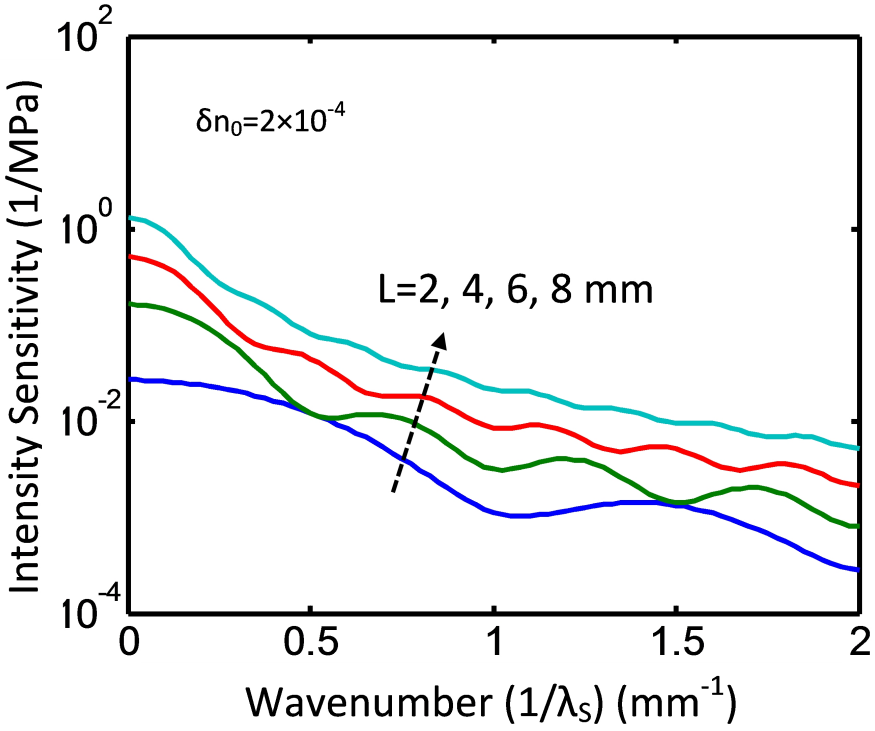

Figure 5.1: Intensity sensitivity of a πFBG with $\delta n_0 = 2 \times 10^{-4}$ under longitudinal waves.

which the wavelength shift is expressed in Eq. 5.9, the geometric effect is just opposite to the strain-optic effect, and the geometric effect dominates; While shear waves, whose vibration direction is perpendicular to the fiber axis, cause little grating period change. Quantitatively comparing the wavelength shift in Eq. 5.9, Eq. 5.19 and Eq. 5.20, we can see that the wavelength shift caused by longitudinal waves are much greater than that caused by shear waves. Besides, the slope of πFBG spectral linear region merely change when ultrasonic waves impinge onto a fiber grating. Therefore, the πFBG sensor has a higher intensity sensitivity when impinged by longitudinal waves than by shear waves. Furthermore, due to the difference of refractive index change in x and y direction caused by shear waves, the intensity sensitivity for πFBG sensors slightly changes when the orientation of input linearly polarized light changes

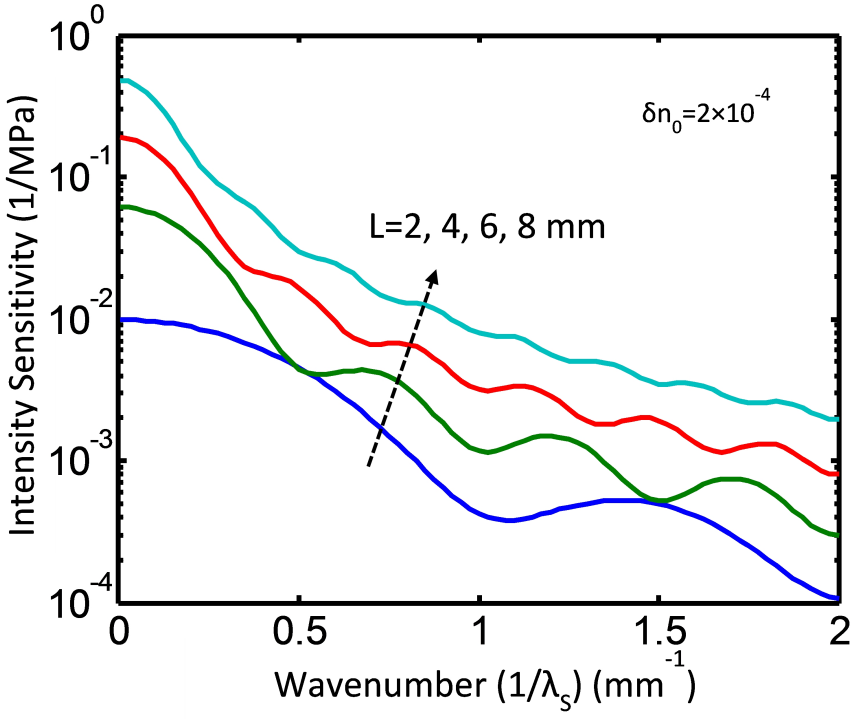

Figure 5.2: Intensity sensitivity of a πFBG with $\delta n_0 = 2 \times 10^{-4}$ under shear waves when a linearly polarized light whose electric field is parallel to x direction is incident to the fiber.

with respect to the fast or slow axis.

5.4 Conclusion

In this chapter, the discussion is extended to ultrasonic longitudinal waves and shear waves. The models of longitudinal waves and shear waves are provided, and grating pitch change and the refractive index changes are derived. For shear waves, the birefringence through the fiber grating is analyzed. Numerical results show that the intensity sensitivities under longitudinal waves are greater than that under shear waves. That different geometric effect and strain-optic effect caused by different types of ultrasonic waves is the reason for the differences of intensity sensitivity.

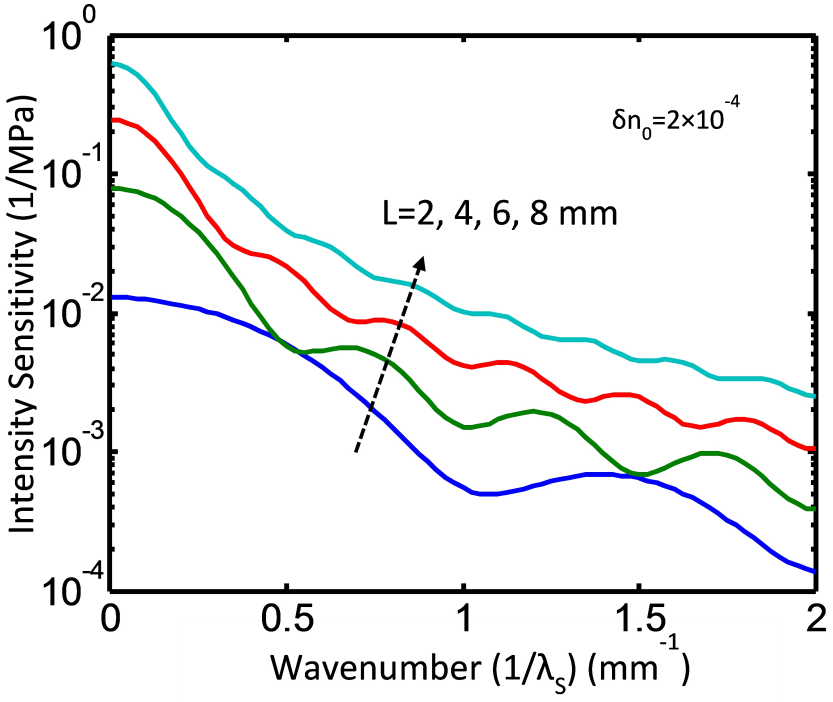

Figure 5.3: Intensity sensitivity of a πFBG with $\delta n_0 = 2 \times 10^{-4}$ under shear waves when a linearly polarized light whose electric field is parallel to y direction is incident to the fiber.

Chapter 6

Conclusion

6.1 Summary

In this thesis, we have carried out extensive numerical simulations to study the responses of uniform FBGs and πFBGs when impinged by ultrasonic pressure waves. A theoretical model has been established to simulate those responses. In the model, the ultrasonic waves is described by a sinusoidal function. The ultrasonic-induced strains are described by the product of strain-optic tensor and strain vectors of different type of ultrasonic waves. Fiber gratings, both uniform FBGs and πFBGs, are modeled by the transfer matrix method, in which the grating is divided into numbers of uniform subsections.

Our simulation results show that, for uniform FBGs and πFBGs, both the wavelength sensitivity and intensity sensitivity decreases as the ultrasonic frequency increases. For both gratings, the wavelength sensitivity can be enhanced by reducing the grating length. For πFBGs only, the wavelength sensitivity can be increased by increasing the refractive index modification depth. In addition, our analysis reveals the intensity sensitivity of a πFBG can be enhanced by increasing the grating length

or the refractive index modification depth. We also analyzed the directivity of a πFBG sensor for pressure waves. When the grating length is smaller than the ultrasonic wavelength, the πFBG is omnidirectional. As the πFBG length increases, the πFBG sensor becomes more directional with the maximum sensitivity occurring at the normal incidence of the ultrasonic wave.

In addition, the grating period change and refractive index change of a πFBG impinged by ultrasonic longitudinal waves or shear waves were calculated. The responses of the πFBG reveal that the πFBG sensors have a higher intensity sensitivity when detecting ultrasonic longitudinal waves than shear waves. Also, the orientation of input light with respect to the vibration direction of shear waves slightly affects the intensity sensitivity due to the different refractive index change in different direction caused by shear waves.

To sum up, our model and analysis have revealed several significant differences between ultrasonic sensors employing uniform FBGs and πFBGs. The results provide an important guidance for designing and optimizing fiber optic ultrasonic sensors utilizing fiber gratings as the sensing element.

Bibliography

[1] I. Perez, H.-L. Cui, and E. Udd, "Acoustic emission detection using fiber bragg gratings," in *Proceedings of SPIE*, 2001. 1.1

[2] D. C. Betz, G. Thursby, B. Culshaw, and W. J. Staszewski, "Acousto-ultrasonic sensing using fiber bragg gratings," *Smart Materials and Structures*, vol. 12, pp. 122–128, 2003. 1.1, 2.1.4

[3] H. Tsuda, "Ultrasound and damage detecton in cfrp using fiber bragg grating sensors," *Composites Science and Technology*, vol. 66, pp. 676–683, 2006. 1.1

[4] D. C. Betz, G. Thursby, B. Culshaw, and W. J. Staszewski, "Structural damage location with fiber bragg grating rosettes and lamb waves," *Structural health monitoring*, vol. 6, pp. 299–308, 2007. 1.1

[5] R. K. Miller and P. McIntire, "Nondestructive testing handbook," *Acoustic Emission Testing*, vol. 5, 1992. 1.1

[6] G. Wild and S. Hinckley, "Acousto-ultrasonic optical fiber sensors: Overview and state-of-the-art," *IEEE Sensors Journal*, vol. 8, pp. 1184–1193, 2008. 1.1, 5.1, 5.1

[7] C. B. Scruby, "An introduction to acoustic emission," *J, Phys. E Sci. Instrum*, vol. 20, pp. 946–953, 1987. 1.1

[8] H. Choi, K. Park, S. Park, U. Paek, B. Lee, and E. Choi, "Miniature fiber-optic high temperature sensor based on a hybrid structured fabry–perot interferometer," *Optics letters*, vol. 33, no. 21, pp. 2455–2457, 2008. 1.1

[9] B. Guan, H. Tam, X. Tao, and X. Dong, "Simultaneous strain and temperature measurement using a superstructure fiber bragg grating," *Photonics Technology Letters, IEEE*, vol. 12, no. 6, pp. 675–677, 2000. 1.1

[10] C. Lawrence, D. Nelson, E. Udd, and T. Bennett, "A fiber optic sensor for transverse strain measurement," *Experimental Mechanics*, vol. 39, no. 3, pp. 202–209, 1999. 1.1

[11] H. Ohno, H. Naruse, M. Kihara, and A. Shimada, "Industrial applications of the botdr optical fiber strain sensor," *Optical fiber technology*, vol. 7, no. 1, pp. 45–64, 2001. 1.1

[12] Y. Zhu and A. Wang, "Miniature fiber-optic pressure sensor," *Photonics Technology Letters, IEEE*, vol. 17, no. 2, pp. 447–449, 2005. 1.1

[13] K. Totsu, Y. Haga, and M. Esashi, "Ultra-miniature fiber-optic pressure sensor using white light interferometry," *Journal of Micromechanics and Microengineering*, vol. 15, p. 71, 2005. 1.1

[14] S. Vohra, P. Bucholtz, and A. Kersey, "A fiber optic dc and low frequency electric field sensor," in *Optical Fiber Sensors*. Optical Society of America, 1992. 1.1

[15] J. Jarzynski and R. De Paula, "Fiber optic electric field sensor technology," in *Society of Photo-Optical Instrumentation Engineers (SPIE) Conference Series*, vol. 718, 1987, pp. 48–55. 1.1

[16] M. Deeter, "Fiber-optic faraday-effect magnetic-field sensor based on flux concentrators," *Applied optics*, vol. 35, no. 1, pp. 154–157, 1996. 1.1

[17] L. Yuan, L. Zhou, and W. Jin, "Long-gauge length embedded fiber optic ultrasonic sensor for large-scale concrete structures," *Optics & Laser Technology*, vol. 36, no. 1, pp. 11–17, 2004. 1.1

[18] P. Fomitchov, T. Murray, and S. Krishnaswamy, "Intrinsic fiber-optic ultrasonic sensor array using multiplexed two-wave mixing interferometry," *Applied optics*, vol. 41, no. 7, pp. 1262–1266, 2002. 1.1

[19] H. Lamela, D. Gallego, and A. Oraevsky, "Optoacoustic imaging using fiber-optic interferometric sensors," *Optics letters*, vol. 34, no. 23, pp. 3695–3697, 2009. 1.1

[20] D. Gallego and H. Lamela, "High-sensitivity ultrasound interferometric single-mode polymer optical fiber sensors for biomedical applications," *Optics letters*, vol. 34, no. 12, pp. 1807–1809, 2009. 1.1

[21] C. Ye and R. Tatam, "Ultrasonic sensing using yb3+/er3+-codoped distributed feedback fibre grating lasers," *Smart materials and structures*, vol. 14, p. 170, 2005. 1.1

[22] S. Løvseth, J. Kringlebotn, E. Rønnekleiv, and K. Bløtekjær, "Fiber distributed-feedback lasers used as acoustic sensors in air," *Applied optics*, vol. 38, no. 22, pp. 4821–4830, 1999. 1.1

[23] N. Fisher, D. Webb, C. Pannell, D. Jackson, L. Gavrilov, J. Hand, L. Zhang, and I. Bennion, "Ultrasonic hydrophone based on short in-fiber bragg gratings," *Applied optics*, vol. 37, no. 34, pp. 8120–8128, 1998. 1.1

[24] A. Kersey, M. Davis, H. Patrick, M. LeBlanc, K. Koo, C. Askins, M. Putnam, and E. Friebele, "Fiber grating sensors," *Journal of Lightwave Technology*, vol. 15, no. 8, pp. 1442–1463, 1997. 1.1

[25] Y. Rao, K. Kalli, G. Brady, D. Webb, D. Jackson, L. Zhang, and I. Bennion, "Spatially-multiplexed fibre-optic bragg grating strain and temperature sensor system based on interferometric wavelength-shift detection," *Electronics letters*, vol. 31, no. 12, pp. 1009–1010, 1995. 1.1

[26] Y. Rao, D. Webb, D. Jackson, L. Zhang, and I. Bennion, "High-resolution, wavelength-division-multiplexed in-fibre bragg grating sensor system," *Electronics Letters*, vol. 32, no. 10, pp. 924–926, 1996. 1.1

[27] P. Fomitchov and S. Krishnaswamy, "Response of a fiber bragg grating ultrasonic sensor," *Optical Engineering*, vol. 42, pp. 956–963, 2003. 1.1, 4.3

[28] M. Majumder, T. Gangopadhyay, A. Chakraborty, K. Dasgupta, and D. Bhattacharya, "Fibre bragg gratings in structural health monitoringŮpresent status and applications," *Sensors and Actuators A: Physical*, vol. 147, no. 1, pp. 150–164, 2008. 1.1

[29] H. Tsuda, K. Kumakura, and S. Ogihara, "Ultrasonic sensitivity of strain-insensitive fiber bragg grating sensors and evaluation of ultrasound-induced strain," *Sensors*, vol. 10, no. 12, pp. 11 248–11 258, 2010. 1.1

[30] J. Lee, H. Tsuda, and B. Koo, "Single-mode fibre optic bragg grating sensing on the base of birefringence in surface-mounting and embedding applications," *Optics & Laser Technology*, vol. 39, no. 1, pp. 157–164, 2007. 1.1

[31] J. Lee, H. Tsuda, and N. Toyama, "Impact wave and damage detections using a strain-free fiber bragg grating ultrasonic receiver," *NDT & E International*, vol. 40, no. 1, pp. 85–93, 2007. 1.1

[32] L. Wei and J. Lit, "Phase-shifted bragg grating filters with symmetrical structures," *Lightwave Technology, Journal of*, vol. 15, no. 8, pp. 1405–1410, 1997. 1.1

[33] E. Chehura, S. James, N. Lawson, K. Garry, and R. Tatam, "Pressure measurements on aircraft wing using phase-shifted fibre bragg grating sensors," in *Proc. SPIE*, vol. 7503, 2009, p. 750334. 1.1

[34] R. Drever, J. Hall, F. Kowalski, J. Hough, G. Ford, A. Munley, and H. Ward, "Laser phase and frequency stabilization using an optical resonator," *Applied Physics B: Lasers and Optics*, vol. 31, no. 2, pp. 97–105, 1983. 1.1

[35] A. Rosenthal, D. Razansky, and V. Ntziachristos, "High-sensitivity compact ultrasonic detector based on a pi-phase-shifted fiber bragg grating," *Optics Letters*, vol. 36, pp. 1833–1835, 2011. 1.1

[36] M. Notcutt, L. Ma, J. Ye, and J. Hall, "Simple and compact 1-hz laser system via an improved mounting configuration of a reference cavity," *Optics letters*, vol. 30, no. 14, pp. 1815–1817, 2005. 1.1

[37] T. Erdogan, "Fiber grating spectra," *Journal of Lightwave Technology*, vol. 15, pp. 1277–1294, 1997. 2.1, 2.2.1, 2.2.1, 2.2.1, 2.2.1, 2.2.1, 2.2.2, 2.2.2, 2.2.2, 3.1.1

[38] G. B. Hocker, "Fiber-optic sensing of pressure and temperature," *Applied Optics*, vol. 18, pp. 1445–1448, 1979. 2.1.1, 2.1.1, 2.1.1, 2.1.2, 2.1.2, 2.1.2

[39] Y.-J. Rao, "In-fibre bragg grating sensors," *Measurement science and technology*, vol. 8, pp. 355–375, 1997. 2.1.3, 2.1.3, 5.1, 5.2

[40] J. L. Rose, *Ultrasonic waves in solid media*, J. L. Rose, Ed. Cambridge University Press, 1999. 2.1.4

[41] K. Okamoto, *Fundamentals of optical waveguides*. Academic press, 2006. 2.2.1

[42] A. Minardo, A. Cusano, R. Bernini, L. Zeni, and M. Giordano, "Response of fiber bragg gratings to longitudinal ultrasonic waves," *IEEE transactions on ultrasonics, ferroelectrics, and frequency control*, vol. 52, pp. 304–312, 2005. 4.2.1

[43] J. Dorighi, S. Krishnaswamy, and J. D. Achenbach, "Response of an embedded fiber optic ultrasound sensor," *J. Acoust. Soc. Am*, vol. 101, pp. 257–263, 1997. 4.5

[44] P. A. Fomitchov, S. Krishnaswamy, and J. D. Achenbach, "Extrinsic and intrinsic fiber optic sagnac ultrasound sensors," *Optical Engineering*, vol. 39, pp. 1972–1984, 2000. 4.5